

1 **Estimating the mass of tephra accumulated on roads to best manage**

2 **the impact of volcanic eruptions: the example of Mt. Etna, Italy**

3 Luigi Mereu^{1,2}, Manuel Stocchi^{1*}, Alexander Garcia¹, Michele Prestifilippo³, Laura Sandri¹, Costanza
4 Bonadonna⁴ and Simona Scollo³

5 ¹Istituto Nazionale di Geofisica e Vulcanologia, Sezione di Bologna, 40100 Bologna, Italy

6 ²CETEMPS Center of Excellence, University of L’Aquila, 67100 L’Aquila, Italy

7 ³Istituto Nazionale di Geofisica e Vulcanologia, Osservatorio Etneo, Sezione di Catania, 95015 Catania, Italy

8 ⁴Department of Earth Sciences, University of Geneva, 1205 Geneva, Switzerland

9 * Now at Department of Earth and Geoenvironmental Sciences, University of Bari “Aldo Moro”, 70125 Bari, Italy

10

11 *Correspondence to:* Luigi Mereu (luigi.mereu@ingv.it)

12 To be submitted to NHESS

13 **Abstract.** Explosive eruptions release significant quantities of tephra, which can spread and settle on the ground, potentially
14 leading to various types of damage and disruption to public infrastructure, including road networks. The quantification of the
15 tephra load is, therefore, of significant interest to evaluate and reduce environmental and socio-economic impact, and for
16 managing crises. Tephra dispersal and deposition is a function of multiple factors, including the mass eruption rate (MER),
17 tephra characteristics (size, shape, density), top plume height (H_{TP}), grain size distribution (GSD) and local wind field. In this
18 work we quantified the tephra mass deposited on the main road network on the east-southeast flanks of Mt. Etna (Italy), during
19 lava fountains occurred in 2021, which are lava jets ejected into the air due to the rapid formation and expansion of gas bubbles
20 within the molten rock, also reaching heights of hundreds of metres. We focused on road connections of municipalities
21 significantly affected by these events such as Milo, Santa Venerina and Zafferana Etnea. First, we analysed a sequence of 39
22 short-lasting and intense Etna’s lava fountains detected by the X-band weather radar, applying a volcanic ash radar retrieval
23 approach that permits us to compute the main eruption source parameters (ESPs), such MER, H_{TP} and GSD. When radar
24 measurements were unavailable for a specific event, we analysed images acquired both by the SEVIRI radiometer and by the
25 visible and/or thermal infrared camera of the Istituto Nazionale di Geofisica e Vulcanologia, Osservatorio Etneo (Catania) to
26 derive the main ESPs. Second, we used the computed ESPs as inputs to run two different numerical models, Tephra2 and

27 Fall3D, and reproduce tephra dispersal and accumulation on the road network. Finally, we produce, for the first time,
 28 georeferenced estimates of tephra mass deposited on the whole road network of three municipalities, allowing us to identify the
 29 main roads which have been mostly impacted by tephra accumulation, as well as to estimate the total mass of primary tephra
 30 that has been removed from roads. Such information represents a valuable input for planning and quick management of the
 31 short-term tephra load hazard for future Etna explosive events.

32 **1 Introduction**

33 The estimation of tephra mass deposited on the ground, following a volcanic explosive eruption, remains a key information
 34 that is not well-covered in the current literature. In fact, tephra dispersal and fallout is by far the most widespread volcanic
 35 hazard affecting both local and distal areas (Jenkins et al. 2015; Barsotti et al., 2018; Bonadonna et al. 2021b) including impact
 36 on public health (Baxter, 1990; Horwell and Baxter, 2006), roofs/building collapse (Spence et al., 2005), dangerous road
 37 conditions (Blong, 1996; Wilson et al., 2012; Jenkins et al., 2014; Blake et al., 2017), contamination of water reservoirs and
 38 vegetation (Wilson et al., 2012; Ágústsdóttir, 2015), damages to electrical infrastructure (Bebbington et al., 2008; Wardman et
 39 al., 2012; Wilson et al., 2012, Dominguez et al., 2021), transportation system disruptions (Casadevall, 1994; Guffanti et al.,
 40 2009; Wilson et al., 2012), and impact on telecommunication networks (Wilson et al., 2012). Even tephra associated with
 41 relatively small intensity eruptions may induce various disrupting effects on transport infrastructure such as aeroplane engine
 42 failure and visibility reduction during both primary tephra fall and ash remobilisation (Sarna-Wojcicki et al., 1981; Bonadonna
 43 et al., 2021b; Johnston and Daly, 1995; Wilson et al., 2014). In particular, tephra accumulation, although not causing
 44 significant physical damage on the road network, can cause wide disruption including reduction of skid resistance, obscuration
 45 of road markings and damage to car air filters (Blake et al., 2016, 2017). Tephra particles are also very abrasive with the degree
 46 of abrasiveness dependent on the hardness of the material forming the particles and their shape and angularity (Blong, 1984;
 47 Johnston, 1997; Labadie, 1994; Heiken et al., 1995; Miller and Casavedall, 1999; Gordon et al., 2005; Wilson et al., 2012;
 48 Blake et al., 2017). Road networks are critical for society under normal operating conditions and especially during
 49 emergencies (e.g. Bonadonna et al. 2021a; Hayes et al. 2022).

50 During volcanic eruptions, routes may be required for the evacuation of residents and to allow emergency services and civil
 51 protection personnel to access the affected areas. The road network is also crucial for both immediate and long-term recovery,
 52 including clean-up and disposal of pyroclastic material, and restoration of services and commerce (Blake et al., 2017).

53 In this work, for the first time, we quantify the tephra mass accumulated on the road network of east and south-east sectors of
 54 Etna, which were more affected during the sequence of explosive events of 2021. Usually, the eruptive sequences at Etna are
 55 characterised by short-lasting explosive events, with duration of few hours, separated by periods that can last from few hours
 56 to few days (Calvari et al., 2018; Andronico et al., 2021; Calvari et al., 2022a). Most studies on exposed critical infrastructure
 57 have focussed on larger events and tephra-fallout accumulations greater than 10 kg/m^2 (Wilson et al., 2012, Blake et al., 2017;

58 Scollo et al., 2013). However, areas around Etna are more frequently impacted by smaller tephra accumulation (Scollo et al.,
59 2013). Limited quantitative data available for explosive activity have hampered a reliable quantification of the impact of the
60 tephra deposition at Etna. To investigate its impact on road networks and better characterise its behaviour, we analysed a
61 sequence of several lava fountains occurred between February 2021 and October 2021, focusing our analysis on 39 events that
62 generated volcanic plumes dispersed by wind mostly towards the east-southeast flanks of the volcano (direction between 90
63 degrees and 130 degrees from North). These episodes began at the South East Crater (SEC) as initial Strombolian activity that,
64 with time, evolved to lava fountain activity, also named paroxysm.

65 Remote sensing is routinely used for monitoring the eruptive activity of Etna; the Istituto Nazionale di Geofisica e
66 Vulcanologia, Osservatorio Etneo (INGV-OE) runs a network of different remote sensing sensors both ground-based (such as
67 thermal infrared and visible cameras) and satellite-based sensors (Scollo et al., 2019). An X-band weather radar located in
68 Fontanarossa airport (Catania), which is part of the monitoring network of the Italian Department of Civil Protection (DPC)
69 allows to monitor and analyse the Etna's eruptions as well (Marzano et al. 2020; Mereu et al. 2020). Using these sensors, we
70 can observe in almost all the cases the temporal evolution of explosive activity and characterise it quantitatively in terms of ma
71 ss eruption rate (MER) and top plume height (H_{TP}). These two parameters are among the main input variables for advection-
72 dispersion models (Scollo et al., 2008a; Biass et al., 2017; Tadini et al., 2022; Takishita et al., 2021), such as Tephra2 and
73 Fall3D (Bonadonna et al., 2005; Costa et al., 2006; Folch et al., 2009, 2020), which have been used in this work to simulate the
74 tephra dispersion and calculate the deposit load at the ground. For each of the 39 events, we estimate the tephra deposited on
75 the road network in order to identify the roads mostly exposed to tephra accumulation and to evaluate the ground mass load that
76 is expected to be removed. Moreover, analysing the simulations done using both models, we investigate their sensitivity to
77 variations of tephra granulometric characteristics and assess the associated uncertainties. The numerical output from a single
78 simulation is a georeferenced map of tephra load, useful to analyse the impact of deposited tephra fallout on roads (Scollo et
79 al., 2009; Scollo et al., 2013; Costa et al., 2012; Bonadonna et al., 2005; Barsotti et al., 2018; Bonadonna et al. 2021a).

80 Analysing tephra accumulation on roads is essential for planning effective responses during volcanic eruptions. By measuring
81 the amount of tephra deposited during both single and multiple eruptions, we can identify which are the roads that are most
82 affected. Moreover, the deposited tephra creates disruptions especially on main roads, considering the large stretches of
83 roadway that may face hazardous driving conditions. This information helps estimate how much material needs to be disposed
84 of and the costs involved in clean up operations. Studying the lava fountain events of Etna in 2021 provides valuable insights
85 for future planning during similar events. By examining the past eruptions, we can predict tephra deposits, providing useful in
86 formation to decision makers to develop better cleaning up strategies. Indeed, for future eruptions, it is important to consider
87 creating a model that uses real-time data to improve predictions and clean up plans. Overall, this research can help crisis
88 management and enhance safety in volcanic regions. Additionally, recent regional legislation (DA n. 8/Gab.
89 22/04/2024, <https://www.regione.sicilia.it>) permits the use of the volcanic tephra for building applications; in this new

90 framework, this study represents an initial effort to estimate the volume of tephra that may be reused rather than disposed of,
 91 transforming a potential problem into a resource.

92 The work is organised as follow: Section 2 provides a brief description of Etna's lava fountain activity; Section 3 presents
 93 ground- and satellite-based sensor data, along with the main eruption source parameters (ESPs) retrieved from them, and the
 94 methodology employed to analyse the model results; Section 4 validates the results against previously published data for a
 95 specific event (February 28th, 2021); Section 5 discusses the modelling outputs and provides conclusive remarks.

96 **2 The lava fountains at Etna in 2021**

97 Etna, one of the most active volcanoes in the world, is a stratovolcano on the east coast of Sicily, Italy. It rises to more than
 98 3,300 m in altitude and has four main summit craters: North-East Crater (NEC), Voragine (VOR), Bocca Nuova (BN) and
 99 South-East Crater (SEC). Between February 2021 and October 2021, approximately sixty paroxysmal episodes occurred from
 100 the SEC. Of these, 39 episodes lasted several hours and were dispersed towards the E-SE (Calvari et al., 2021).

101 Lava fountains, which are formed by a hot inner core consisting of a mix of liquid clots, pyroclasts, and magmatic gases, are
 102 often observed during paroxysmal episodes at Etna and can rise several hundred metres above the volcanic vent
 103 (Wilson et al., 1995; Taddeucci et al., 2015). Moreover, during those events it is likely that an eruption column of almost 10-15
 104 km above sea level can form above the lava fountains.

105 Usually, lava fountains are divided in three phases (e.g., Alparone et al., 2003; Mereu et al., 2020; Calvari et al., 2022b): 1)
 106 Resumption phase, which commonly begins with slow initial effusion from the vent, followed by a progressive increase in
 107 explosive activity; 2) Paroxysmal phase, lasting from 10 to 120 minutes, during which there is a rapid transition from
 108 Strombolian activity to sustained lava fountains that rise up an altitude of 2-6 km above the vent; 3) Conclusive phase, during
 109 which the eruptive episode gradually ceases .

110 **3 Methods**

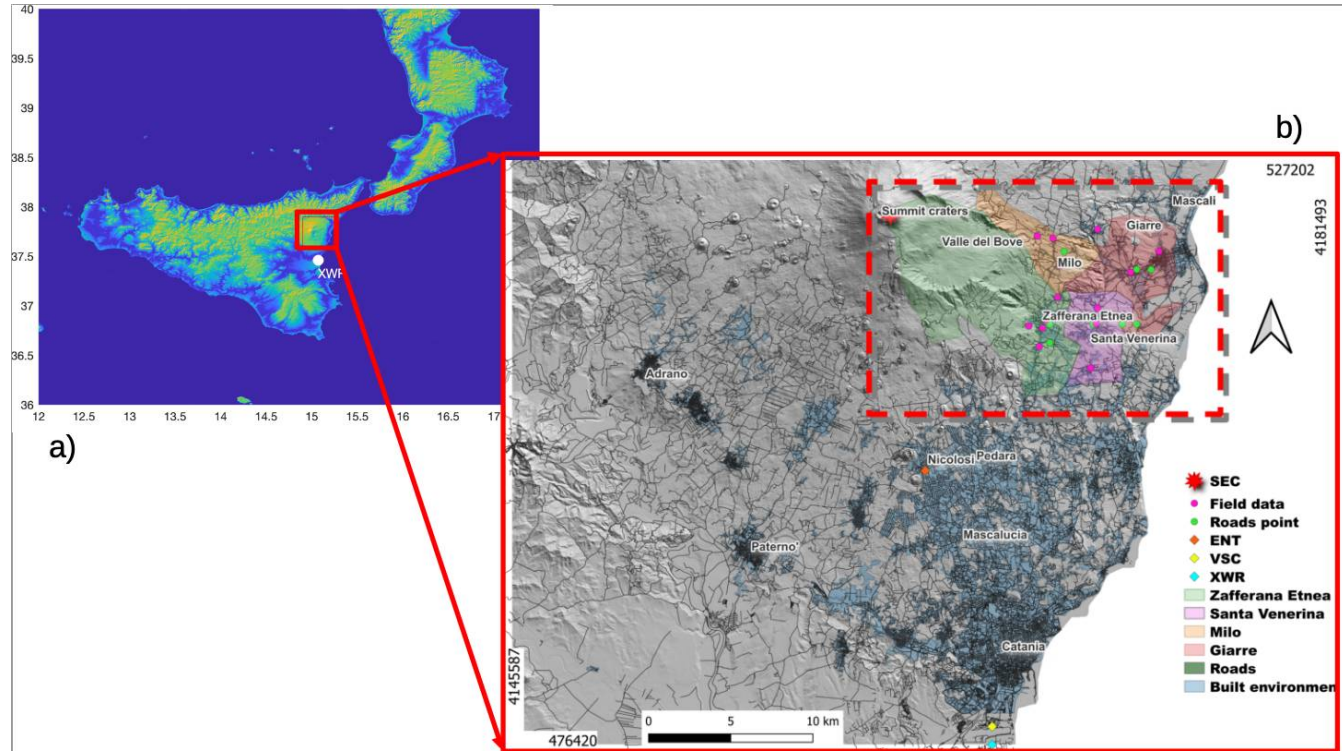
111 **3.1.1 Sensors and outputs**

112 For the analyses in this work we select all the Etna eruptions characterised by a tephra plume dispersed towards east-southeast
 113 flanks of the volcano. These events, listed in Table 1, have been observed using different sensors that are briefly described
 114 below:

115 a) X-band Weather Radar (XWR), located in the airport of Catania, 32 km at SSE Etna summit craters (Figure 1). The scanning
 116 agility in elevation and azimuth of this sensor allows it to probe the tephra cloud in any weather condition and both during the
 117 day and night (Mereu et al., 2022, 2023; Montopoli, 2016; Vulpiani et al., 2016). Applying the Volcanic Ash Radar Retrieval
 118 (VARR) methodology (e.g. Marzano et al., 2012, 2020; Mereu et al., 2015, 2020) to measure radar reflectivity factor, we

119 estimate: i) the top plume height H_{TP} (km) above sea level, which is the maximum height reached by the eruption column,
120 calculated as the maximum altitude of the radar-detected volume above the volcanic vent contaminated by the minimum
121 detectable tephra concentration; ii) the mass eruption rate Q_M (kg/s), that is estimated by the time-space variation of tephra
122 concentration detected above the Etna summit probing the volcanic plume; iii) the total erupted mass TEM (kg), which is the
123 total mass of pyroclastic material erupted during the explosive event; the ash-fall rate Ra ($\text{kg}/\text{m}^2 \cdot \text{h}$) useful to derive the tephra
124 load integrating this quantity over a time interval and assuming that the radar measurements closer to the ground are indicative
125 of tephra deposited on the ground from the vertical column above a considered position (Mereu et al., 2015).
126 b) Etna Catania Visible calibrated camera (ECV), located in Catania about 30 km from Etna summit craters (Scollo et al., 2019;
127 Aravena et al., 2023, Figure 1); it allows us to monitor the altitude of dispersed plume during the light hours when the visibility
128 is not compromised by the meteorological cloud cover. In this way, we can derive the time sequence of H_{TP} .
129 c) Spinning Enhanced Visible and InfraRed Imager (SEVIRI), on board of Meteosat Second Generation (MSG) satellites, is a
130 multispectral radiometer which produces daytime brightness temperature (BT) images with 3 km resolution. Selecting the BT
131 along the Etna summit in the channel of $10.8 \mu\text{m}$, that is more sensitive to the tephra dielectric signature, we infer H_{TP} looking
132 for the altitude in which the detected BT can be found in the temperature profile as a function of altitude, which is derived from
133 the hydro-meteorological service of Agenzia Regionale Prevenzione e Ambiente (ARPA) in Emilia Romagna (Scollo et al.,
134 2009; Romeo et al., 2023).
135 d) Etna Nicolosi Thermal (ENT) infrared camera, located in Nicolosi at about 15 km from Etna summit (Figure 1), which
136 measures the thermal activity associated with lava fountains. It is worth highlighting that when the radar measurements were
137 not available and the volcanic plume was not easily detectable by the satellite sensor or by the visible calibrated camera,
138 analysing the ENT images we have identified the Incandescent Jet Region (IJR), which is a proxy of the lava fountain height.
139 As described in Mereu et al., (2020), the time sequence of maximum height of IJR area can be converted in exit velocity $v_{ex}(\text{m/s})$
140 of pyroclastic material, using the Bernoulli equation under the following approximations: i) most of the pyroclastic material
141 is sufficiently large to be considered as accelerated projectiles confined in this IJR; ii) atmospheric density variations and drag
142 effects are negligible. Assuming a trustworthy value of tephra-gas mixture density and of surface vent, we can deduce Q_M
143 applying the surface flow approach (SFA) described in Marzano et al., (2020) and Mereu et al., (2022). It is worth noting that H_{TP}
144 obtained from various sensors, such as XWR, ECV, and SEVIRI, exhibits a comparable time trend, as shown in Freret-
145 Lorgeril et al. (2021) and Scollo et al. (2019). The complete ESPs dataset for each of the Etna events considered in this study
146 is displayed in Table 1. Real-time estimation of ESPs can be challenging, especially during the initial phase, increasing the
147 uncertainty in short-term forecasts of plume dispersal (Scollo et al., 2008a). Furthermore, we also collected qualitative
148 information about the eruptions, such as plume height (based on VONA reports; Scollo et al., 2019; Corradini et al., 2018), the
149 presence of tephra fallout and the start and end times of Strombolian and lava fountain activities (based on bulletins and reports
150 available on the INGV-OE website (www.ct.ingv.it)).

151



152

153 **Figure 1: (a) Map of South Italy (Sicily and Calabria), with the red square showing the Etna area framed in the right panel; (b) georeferenced map of road network (dark lines) of the Etna volcano area(shapefiles with the road data is publicly available from the Regione Sicilia website: <https://www.regione.sicilia.it/>). The UTM coordinates (area 33S) are shown in the lower-left part and in the upper-right part of the picture, respectively. The areas of four municipalities, of which three are under examination, and the built environment are highlighted with different colours, whereas each sensor, field data and road points are identified by coloured symbols as listed in the legend in the right side: ground-based sensors employed in this work (the visible camera VSC, the thermal infrared camera ENT and the X-band radar XWR); the South East Carter SEC; 14 field data as derived by Pardini et al. (2021); 8 road points. The rectangle highlighted with the dotted red line identifies the area examined and focused in Figures 3 and 7.**

162 On the other hand, each sensor previously described allows us to measure some features of the lava fountains, which need
 163 further elaborations to obtain the ESPs. In this work, H_{TP} (km) and Q_M (kg/s) quantities are directly derived by processing
 164 XWR measurements. When it was not possible to determine H_{TP} from XWR, ECV frames or SEVIRI data, we used the ENT
 165 images to retrieve the Q_M estimates applying the SFA (Marzano et al. 2020; Mereu et al., 2022). Integrating the SFA in time,
 166 we obtain TEM (kg), whereas applying the empirical relation of Mastin et al. (2009), which links Q_M to H_{TP} , we get the H_{TP} a
 167 bove the Etna summit crater (which is located about 3357 m above sea level). We used the inverse Mastin equation in those
 168 cases where the H_{TP} was derived from VSC or SEVIRI imagery to obtain the Q_M time sequence. The starting and ending time

12

169 for each Etna explosive eruption can be straightly inferred selecting the ends of time range from: i) XWR-based Q_M estimates,
 170 where $Q_M > 5 \cdot 10^5$ kg/s; ii) temporal range where ENT camera identifies the lava fountaining feeding the explosive phase; iii)
 171 time range in which a quick development of the volcanic cloud is observed by the ECV frames or SEVIRI images. Regarding
 172 the wind data, while for Tephra2 simulations we consider a horizontally-constant wind field computed as the mean wind
 173 velocity between the Etna summit craters and the maximum value of the H_{TP} sequence, for Fall3D simulations we use the
 174 whole meteorological profile. This data, which is used to feed the ash dispersion models, are derived from the European
 175 Centre for Medium-Range Weather Forecasts (ECMWF) ERA5 reanalysis
 176 (<https://www.ecmwf.int/en/forecasts/datasets/reanalysis-datasets/era5>). The grain-size distribution usually refers to the
 177 volcanic particle size, indicated by the relation $\phi = -\log_2(D)$, where D stands for sphere-equivalent mean diameter (measured
 178 in mm). The ϕ refers to the whole deposit, assumed as a Gaussian distribution characterised by a maximum, minimum, mean
 179 and standard deviation. In order to consider all possible cases, in this work we vary the median ϕ value between -1 to +1 with
 180 a step of 0.5. The georeferenced location and the elevation of the SEC are considered to complete the set of input parameters
 181 used, as listed in Table 1. It is worth noting that for each event listed in Table 1, we consider the UTM coordinates of the vent
 182 in easting (500024.03 m) and northing (4177699.5 m), or, equivalently, in longitude (15.000273°E) and latitude
 183 (37.746592°N), we assume a ϕ with maximum, minimum and standard deviation values equal to -6, 10 and 3, respectively; we
 184 repeat each simulation, varying the median ϕ values, so that we obtain a total of 195 simulations from each numerical model.
 185

186 **Table 1. Input parameters used for setting the numerical dispersion model Tephra2 and Fall3D: starting time and ending time of**
 187 **paroxysm (dd:mm:yy, hh:mm), duration Δt (s), top plume height H_{TP} (m) above sea level (a.s.l.) and above volcano vent (a.v.v.), total**
 188 **erupted mass TEM (kg).**

189

START TIME Date T0 UTC	END TIME Date T=T0+Dt UTC	Δt [s]	H_{TP} (a.s.l.) [m]	H_{TP} (a.v.v.) [m]	TEM [10 ⁷ kg]
17/02/21 23:40	18/02/21 01:20	6000	9300	5943	18
19/02/21 08:40	19/02/21 10:30	6600	10000	6643	29
28/02/21 07:50	28/02/21 09:50	7200	11900	8543	250
07/03/21 06:20	07/03/21 07:50	5400	11600	8243	110
12/03/21 05:50	12/03/21 10:50	18000	10500	7143	175
14/03/21 23:20	15/03/21 02:20	10800	10957	7600	540
17/03/21 02:50	17/03/21 05:10	8400	6300	2943	22
19/03/21 08:40	19/03/21 10:20	6000	10400	7043	98
19/05/21 03:00	19/05/21 04:30	5400	5000	1643	0.09

22/05/21 20:20	22/05/21 22:40	8400	11057	7700	445
24/05/21 20:30	24/05/21 22:45	8700	11000	7643	468
28/05/21 06:20	28/05/21 07:50	5400	10857	7500	0.4
28/05/21 18:10	28/05/21 21:10	10800	10757	7400	486
30/05/21 03:00	30/05/21 06:00	10800	7500	4143	46.9
02/06/21 08:10	02/06/21 10:50	9600	7600	4243	13.2
04/06/21 16:40	04/06/21 18:40	7200	7500	4143	10
12/06/21 18:30	12/06/21 19:10	2400	9000	5643	17.7
14/06/21 21:40	14/06/21 22:30	3000	6300	2943	56
16/06/21 10:30	16/06/21 13:00	9000	8000	4643	15.8
17/06/21 22:40	17/06/21 23:55	4500	12457	9100	290
20/06/21 22:40	21/06/21 00:40	7200	10900	7543	18
22/06/21 03:30	22/06/21 04:20	3000	8000	4643	11.8
23/06/21 02:00	23/06/21 03:40	6000	7300	3943	77
23/06/21 17:40	23/06/21 19:00	4800	11500	8143	120
24/06/21 09:20	24/06/21 11:00	6000	12200	8843	4.2
25/06/21 18:20	25/06/21 19:40	4800	10664	7307	4.8
25/06/21 00:30	25/06/21 02:40	7800	10616	7259	230
26/06/21 15:20	26/06/21 17:20	7200	9000	5643	22
27/06/21 08:50	27/06/21 10:00	4200	10000	6643	72.9
28/06/21 14:30	28/06/21 15:40	4200	10000	6643	68.8
01/07/21 23:40	02/07/21 01:40	7200	11109	7752	396
04/07/21 15:00	04/07/21 17:50	10200	8200	4843	8.8
06/07/21 22:00	06/07/21 23:45	6300	10000	6643	190
20/07/21 06:20	20/07/21 08:30	7800	11800	8443	79
31/07/21 21:00	31/07/21 23:50	10200	11000	7643	309
09/08/21 02:00	09/08/21 04:40	9600	12000	8643	140
29/08/21 16:40	29/08/21 18:00	4800	9000	5643	13.1
21/09/21 07:30	21/09/21 09:20	6600	10900	7543	47
23/10/21 08:40	23/10/21 11:30	10200	12300	8943	240

190 3.2 Models

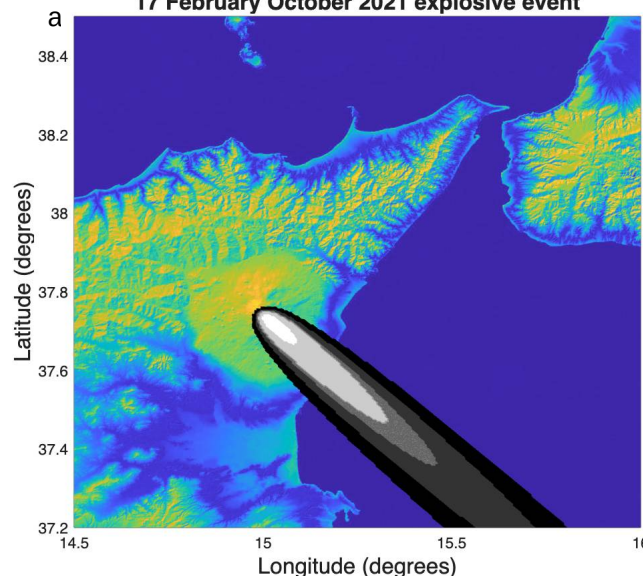
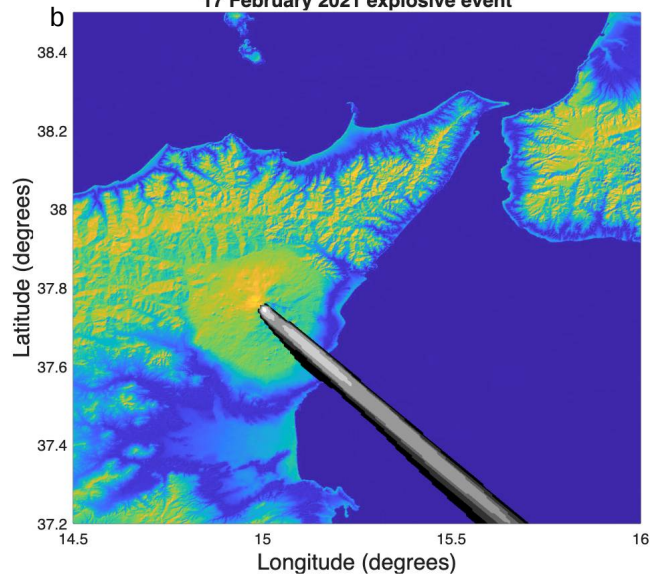
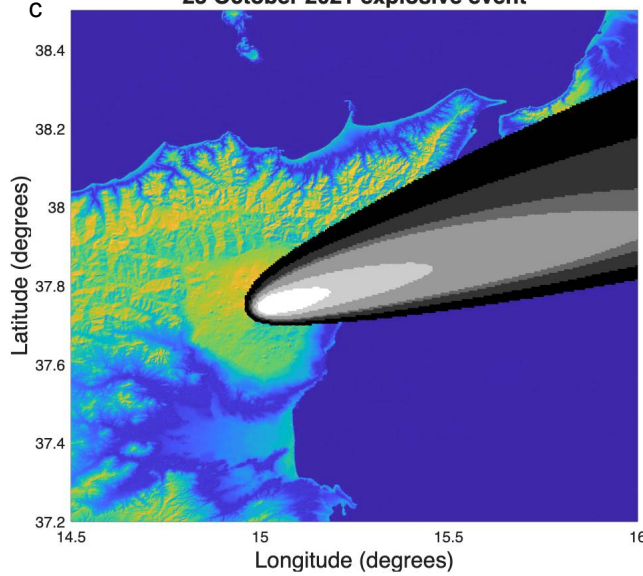
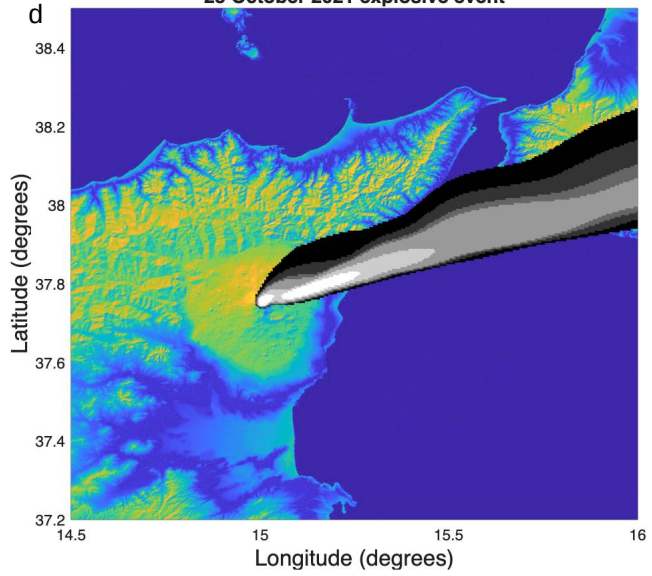
191 3.2.1 Modelling tephra fallout

192 In this study, we simulate the transport, dispersal and deposition of tephra with two different numerical Eulerian models: a
 193 semi-analytical model Tephra2 and a full computational model Fall3D. We run both models on a grid covering the area (14.5°
 194 long, 37° lat) and (16° long, 38.5° lat) with a spatial resolution of ~500 m. Tephra2 allows to evaluate the ground tephra
 195 deposition employing the advection-diffusion theory (Bonadonna et al. 2005, 2006; Connor and Connor, 2006; Volentik et al.
 196 2009; Biass et al. 2016, 2017) taking as inputs: H_{TP} ; TEM; ϕ ; the density of lithics and juveniles (volcanic particles released
 197 from the column, which varies widely from ~500 kg/m³ in highly vesicular clasts to ~2700 kg/m³ in dense ones); the diffusion
 198 coefficient (K), which accounts for atmospheric processes including atmospheric diffusion and cloud gravitational spreading;
 199 the fall time threshold (FTT), an empirical threshold that defines the transition between two different laws of atmospheric
 200 diffusion and the plume ratio (PR), factor describing the mass distribution in the plume, a horizontally uniform wind field. In
 201 the Tephra2 model, it is assumed that a vertical eruption column forms above the vent. The column is discretized, and particles
 202 fall from every part of its height. The total tephra mass is vertically distributed within the eruption column according to a
 203 probability density function that represents mass as a function of height. The model provides three different mass distributions:
 204 uniform, log-normal, and beta distribution. The total grain size distribution for the eruption is estimated assuming a normal
 205 distribution in ϕ units (Bonadonna et al., 2005).

206 Fall3D (v8.0, Folch et al., 2020) models both the particle concentration in the atmosphere (i.e. tephra cloud evolution) and the
 207 particle loading at ground level, based on a 3-D time-dependent Eulerian scheme (Costa et al., 2006; Folch et al., 2009; Folch
 208 et al., 2012). The model solves the advection-diffusion-sedimentation (ADS) equation over a topographical 3D domain, with
 209 several modelling options, including particle aggregation and source terms, among others. The meteorological data used in the
 210 simulations are obtained by interpolating the outputs of a meteorological model into the simulation domain. The simulations
 211 conducted for this work were performed with no aggregation, using the one-dimensional buoyant plume theory (Folch et al.,
 212 2016) as a model for the source term. The meteorological data were retrieved from the ECMWF ERA5-Reanalysis database
 213 (Hersbach et al, 2018). This methodology has the potential to track the evolution of particle concentration during an eruption,
 214 but the main limitation is the computational cost (Costa et al., 2006). Fall3D uses the same ESP's inputs listed in Table 1, but
 215 instead of TEM, it considers Q_M . Figure 2 shows the simulated tephra load (kg/m²) maps for two among the largest-TEM
 216 eruptions (10^8 kg and 10^9 kg), assuming $\phi=0.5$. Generally, we note a greater spreading of tephra deposition to the ground
 217 simulated by Tephra2 with respect to Fall3D. Both numerical models generate output files in netCDF format (e.g.
 218 <https://www.unidata.ucar.edu/software/netcdf/>) containing geo-referenced data on tephra load (kg/m²) on the ground in UTM
 219 coordinates (zone 33-S for Etna) with a grid spacing of 500 m. The limitations of both models, as a function of variation of
 220 input parameters listed in Table 1, as well as and considerations of topography, column mass distribution models, bulk particle
 221 shape, and particle terminal fall velocity, are described in detail in Scollo et al.(2008b).

222

223

17 February October 2021 explosive event**17 February 2021 explosive event****23 October 2021 explosive event****23 October 2021 explosive event**

232

233

234

235

236

237

238

239

240

241

242

243

244

245

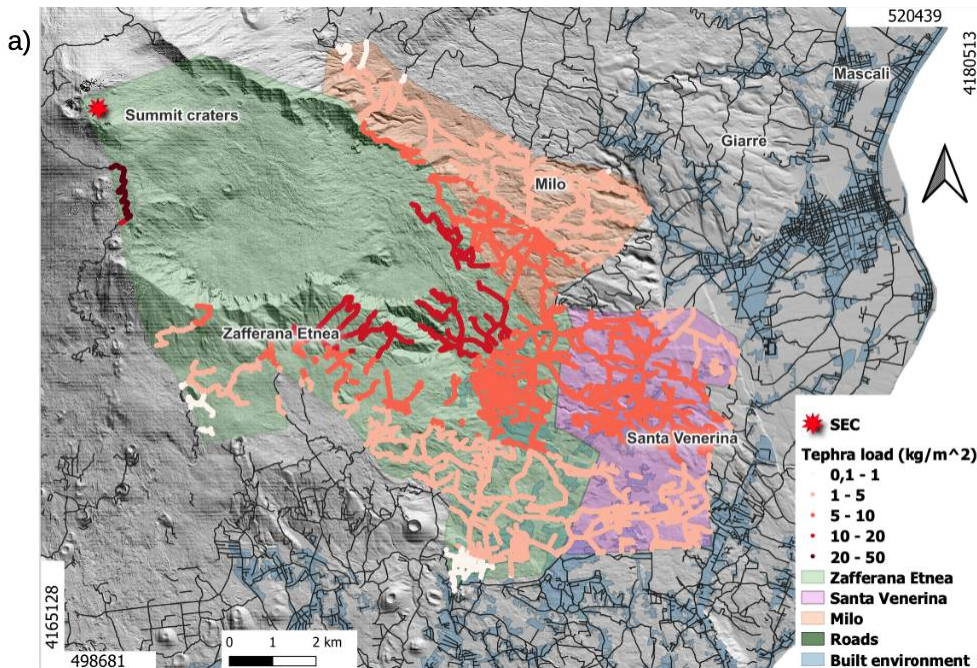
246

Figure 2: Maps of tephra load (kg/m^2) for the Etna lava fountain event of 17 February 2021 (a-b) and of 23 October 2021 (c-d)), using the Tephra2 (a-c)) and Fall3D (b-d)) models. Tephra deposition is plotted as uniform iso-mass contour lines in grayscale, ranging from black for values lower than 10 kg/m^2 to light white for values greater than $5 \cdot 10^3 \text{ kg/m}^2$. The colour scale is the same in all panels.

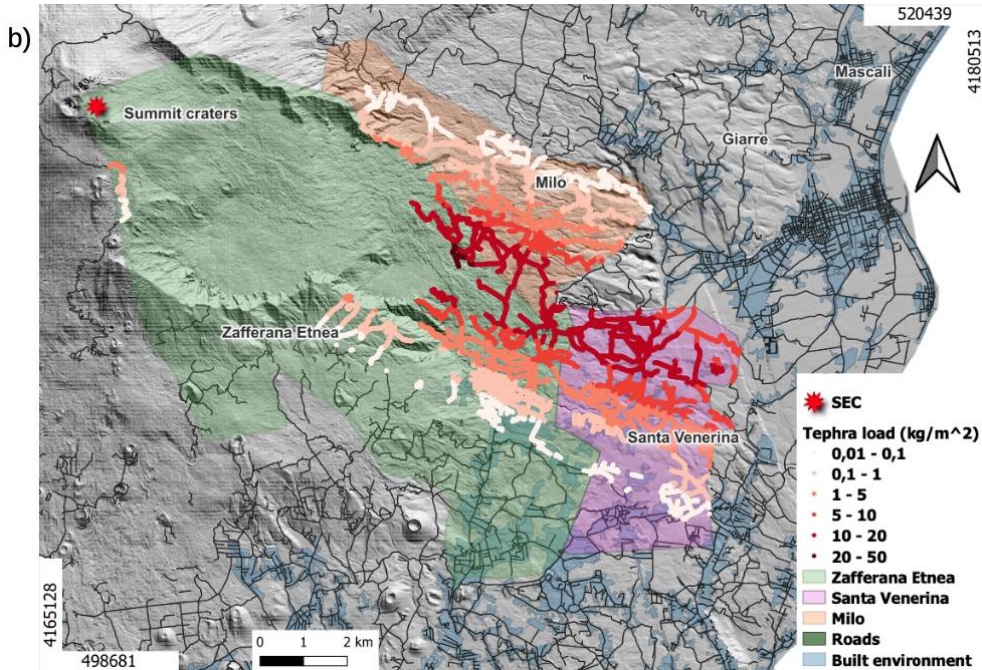
247 3.2.2 Calculating the tephra load and mass on the road network

248 Since our main interest in this work is to calculate the tephra load in the road network, we increase the grid spacing of the
 249 tephra load data to 5 m using linear interpolation. Afterwards, we use the Quantum Geographical Information System (QGIS)
 250 tool to determine the intersection between the downscaled tephra load data and the areas covered by the road network. While
 251 the tracks of road network in the study area is publicly available (geospatial vector data in shapefile format, as shown in Figure
 252 1, from the Regione Sicilia; website <https://www.regione.sicilia.it/>), an accurate estimate of area of roads is not still available
 253 . In order to estimate the area of the roads, we selected several roads in the study area and measured their width using both QG
 254 IS integrating an OpenStreetMap layer (<https://wiki.openstreetmap.org/wiki/QGIS>), and satellite images from GoogleEarth
 255 (<https://earth.google.com/web/>), obtaining an average width of approximately 6 m. Assuming that the roads are generally
 256 composed of two carriageways, this value is in agreement with the prescribed widths for urban and extra-urban roads
 257 according to the Italian law on roads (art. 2 del Testo Unico, which ranges from 2.8 m and 4 m per carriageway). To consider an
 258 uncertainty in this gross measurement, we set the road width to 6 ± 0.5 m. The case study is focused on the road networks
 259 located within the municipal area of Milo, Santa Venerina and Zafferana Etnea towns. For a given road segment we calculate
 260 the corresponding road area (m^2) and then using the tephra load (kg/m^2) we calculate the total mass (kg) deposited on each road
 261 segment. Figure 3 (which covers the area in the rectangle shown with a dotted red line in Figure 1) shows the simulated tephra
 262 load (kg/m^2) on the geo-referenced road network within the Milo (light orange area), Santa Venerina (light pink area) and
 263 Zafferana Etnea (light green area) municipalities for the event on 28 February 2021.

264



265



266

267 **Figure 3: Tephra load (kg/m^2) on the road network of Milo, Santa Venerina and Zafferana Etnea municipalities computed for**
 268 **the Etna explosive event on 28 February 2021, assuming $\phi = 0.5$ and using both Tephra2 (a) and Fall3D (b) models. The tephra**
 269 **deposits in the road graph are shown in red scale for selected threshold levels of the tephra load values (as shown in the legend).**

270 **4. Results**

271 **4.1 Validation: case study on February 28, 2021**

272 In order to verify the results obtained in this study, we focus our attention on the case study of the event on 28 February 2021,
 273 which has been observed by the XWR and analysed by Pardini et al. (2021). Table 2 shows the coordinates (longitude, latitude)
 274 of 14 points in which field measurements of tephra load are available (from literature, e.g., Pardini et al., 2021) in the selected
 275 municipalities (see Figure 1) as well as the results of tephra load derived from the Tephra2 and Fall3D models, fixing the ϕ to
 276 0.5. The XWR retrievals are obtained considering the tephra load rate ($\text{kg}/\text{m}^2 \text{ s}$) related to the first four elevations, which is
 277 equal to a few km of altitude with respect to the ground, and integrating it for the whole time sampling of the radar. In this way
 278 we can retrieve the tephra load (kg/m^2) related to the whole lava fountain. The correlation between the ground field data
 279 (Pardini et al., 2023) and the estimated values using Tephra2, Fall3D, and XWR are plotted, respectively, in Figure 4a, 4b, and
 280 4c. We observe that taking as reference the observed values reported by Pardini et al., 2023, Tephra2 tends to overestimate wh
 281 ile Fall3D tends to underestimate the tephra load values. This is evident from the majority of the points dispersed above and

282 below the bisector, as well as from the differences in the slope of the regressive curves with respect to the bisector shown in
283 Figures 4a and 4b. These discrepancies could be due to different dispersal settings used in the numerical model. In contrast, a
284 good correlation between field data and XWR data is observed (Figure 4c), where the points mostly distribute around the
285 bisector and the regressive straight line is almost parallel to it.

286 To evaluate the degree of agreement between field data and tephra load estimates, we implemented a non-parametric test
287 (namely the Kendall's tau correlation). Table 3 summarises Kendall's tau coefficients, the p-values for testing the null
288 hypothesis of no correlation against the alternative hypothesis of a non-zero correlation; moreover, we estimate the mean
289 absolute percentage error (MAPE) between predicted/estimated data and the observed field data. A Kendall's tau value closer
290 to 1 indicates a better correlation between the field data and the model/estimate data, whereas a low p-value (<1%) indicates a
291 significant correlation.

292 This test confirms that the estimates of both XWR and Tephra2 exhibit a better correlated variation with the field
293 measurements, as indicated by the respective higher tau and lower p-values. The MAPE calculation further supports this
294 conclusion.

295 **Table 2. Etna eruption on February 28, 2021: tephra load (kg/m²) on 14 sites, each one identified by the latitude and longitude, as**
296 **deduced by Pardini et al. (2021), and in the same points as derived by Tephra2 and Fall3D models (fixing $\phi = 0.5$) and retrieved by**
297 **XWR.**

298

Coordinates (degrees)		Tephra load (kg/m ²)			
Longitude	Latitude	Tephra2	Fall3D	XWR	Field data
15.102649	37.677930	5.0	0.0	2.4	1.0
15.095485	37.689185	9.0	0.0	4.1	3.3
15.104990	37.688067	8.9	0.2	4.3	3.3
15.107469	37.692398	8.7	1.1	7.6	6.2
15.115397	37.704832	9.1	16.8	8.4	4.7
15.117104	37.722241	4.0	1.9	6.7	4.3
15.112271	37.737129	1.6	0.0	3.5	2.4
15.101504	37.738418	1.6	0.1	3.5	2.1
15.143073	37.742075	0.2	1.7	1.6	0.1
15.165928	37.718516	1.3	0.0	2.3	1.5
15.141991	37.690479	6.4	10.5	3.4	3.9
15.138243	37.666113	4.4	0.0	1.0	1.0
15.142994	37.698936	5.6	13.1	3.1	4.6
15.185512	37.729891	0.2	1.4	0.5	0.5

306 **Figure 4:**
 307 the
 308 points
 309 field data
 310 2023) as a
 311 results
 312 Fall 3D
 313 results
 314 green
 315 in Table 2
 316 shown in
 317 and c).
 318 dark
 319
 320 bisector, while the magenta line represents the regressive straight line.

Tephra load
 correlation:
 coloured
 represent the
 (Pardini et al.,
 function of the
 from Tephra2,
 and XWR
 (blue, red and
 dots), as listed
 and
 respectively
 panel a), b),
 The dashed
 represents the

322

323 **Table 3.** Kendall's tau correlation coefficient, p-value, and Mean Absolute Percentage Error (MAPE) computed for the Etna
 324 eruption on February 28, 2021

Kendall method	τ	p-value	MAPE
T2-Field data	0.73	$2.8 \cdot 10^{-3}$	48
F3-Field data	0.54	$4.56 \cdot 10^{-2}$	$3.7 \cdot 10^4$
XWR-Field data	0.84	$1.3 \cdot 10^{-4}$	34

325

303
 304
 28

326 Assuming the width of (6 ± 0.5) m for each road, we convert the tephra load to tephra mass (kg) for the event of 28 February
 327 2021, assuming $\phi = 0.5$. We selected a few roads, characterised by their larger extension, for each municipality: Via Bellini and
 328 Corso Italia in Milo; via Mazzini, via Galimberti and via Stabilimenti in Santa Venerina; via Libertà, via Zafferana Milo and
 329 via delle Rose in Zafferana Etnea. We summarise in Table 4 the total tephra mass for streets of Milo, Santa Venerina and
 330 Zafferana Etnea as derived from Tephra2 and Fall3D models. The total mass computed for the selected roads in Milo by
 331 Tephra2 and Fall3D shows a comparable order of magnitude (10^7 kg), whereas for two selected roads in Zafferana Etnea
 332 reveals a disagreement of one order of magnitude. However, the values computed for all municipalities show a maximum
 333 variability between approximately five times the tephra deposit collected on the ground (Scollo et al., 2007). The Tephra2
 334 outcomes are generally larger than those of Fall3D, with the ratio between Fall3D and Tephra2 ranging from 0.3 to 1.4 for the
 335 roads and from 0.3 to 1.1 for towns. The variability in road width corresponds to a variability in tephra mass of approximately
 336 $\pm 9\%$. The last three rows in Table 4 show the total mass computed on the whole road network of the three municipalities,
 337 highlighting the comparable results (same order of magnitude of about 10^9 kg). It is worth noting that the total mass derived
 338 from Tephra2 in Zafferana Etnea municipality is four times larger than the total mass derived from Fall3D. This variability can
 339 be observed in Figure 3. Not all roads are affected by tephra load, as shown in Figure 3b, and this can be attributed to
 340 dissimilarity in the dispersal laws implemented in each model (Scollo et al., 2008; Bonadonna et al., 2005; Folch et al., 2012,
 341 2016). It is important to note that during a typical explosive event at Etna, only a few kilograms of tephra accumulate on a
 342 limited number of streets across the three municipalities. This aspect is closely related to the intensity of the explosive event,
 343 the amount of pyroclastic material erupted, and the wind dispersal pattern.

344

345 **Table 4. Total tephra mass (kg) computed on main roads selected of Milo, Santa Venerina and Zafferana Etnea for the Etna**
 346 **eruption on 28 February 2021 as derived from the results obtained using Tephra2 and Fall3D models (fixing $\phi=0.5$ and assuming a**
 347 **road width of 6 ± 0.5 m). The total mass on the road network of Milo, Santa Venerina and Zafferana, for three road widths (5.5 m, 6**
 348 **m, and 6.5 m), is presented in the last three rows. On the right column the mass ratio between Fall3D and Tephra2 results.**

349

Lava fountains on 28 February 2021	Total tephra mass (10^7 kg)		
Location	Tephra2 (5.5, 6, 6.5 m-width road)	Fall3D (5.5, 6, 6.5 m-width road)	Mass Ratio
Milo-Via V. Bellini	2.4, 2.6, 2.9	1.3, 1.4, 1.6	0.5
Milo-Corso Italia	1.4, 1.6, 1.7	1.7, 1.9, 2.1	1.2
S. Venerina-Via G. Mazzini	0.02, 0.2, 0.2	0.01, 0.1, 0.1	0.5
S. Venerina-Via D. Galimberti	9.7, 10.6, 11.5	9.8, 10.7, 11.6	1.0
S. Venerina-Via Stabilimenti	0.1, 0.4, 0.5	0.2, 0.8, 1.0	2
Zafferana E.-Via Libertà	2.7, 3.0, 3.2	3.9, 4.3, 4.6	1.4
Zafferana E.-Via Zafferana Milo	1.0, 1.1, 1.2	0.3, 0.3, 0.3	0.3
Zafferana E.-Via delle Rose	1.6, 1.8, 1.9	0.4, 0.5, 0.5	0.3

Total mass on the municipality's road network			
Milo	170.0, 185.4, 209.1	131.4, 143.3, 155.3	0.8
Santa Venerina	129.6, 141.4, 153.2	144.1, 157.2, 170.3	1.1
Zafferana Etnea	659.1, 719.0, 779.0	165.2, 180.2, 195.2	0.3

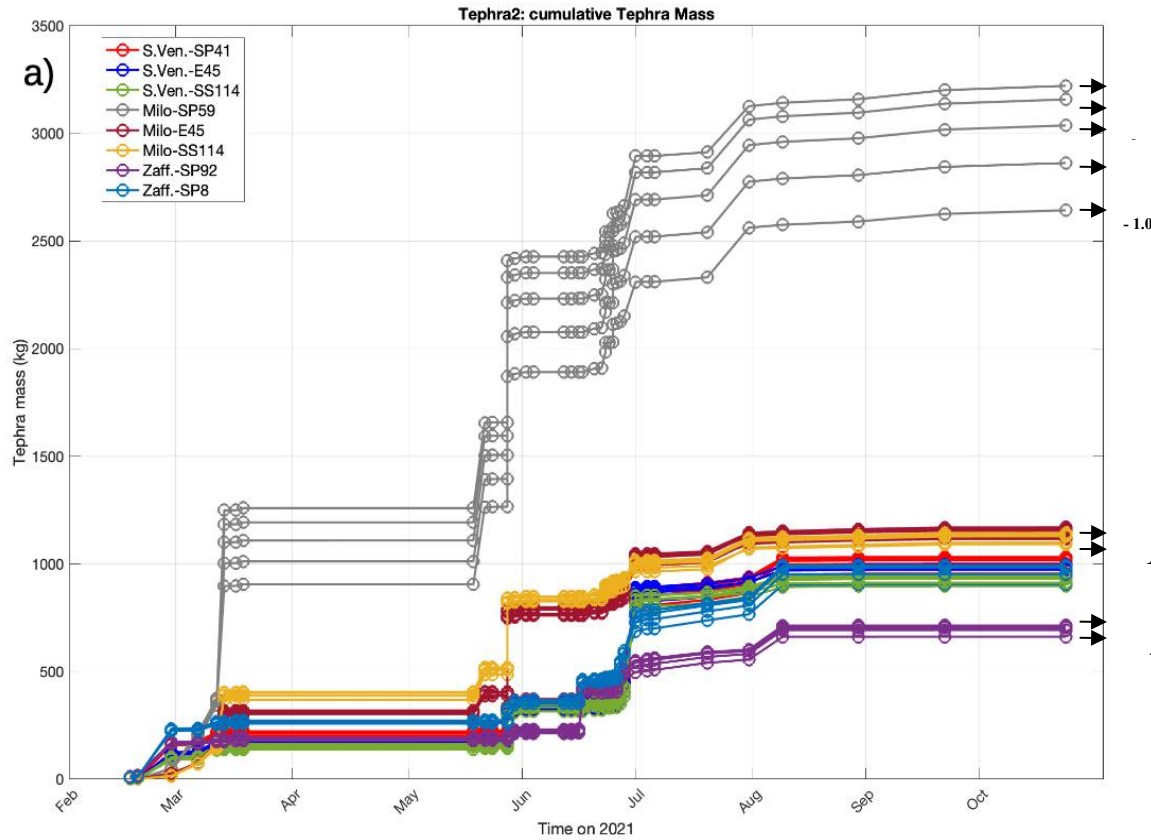
350

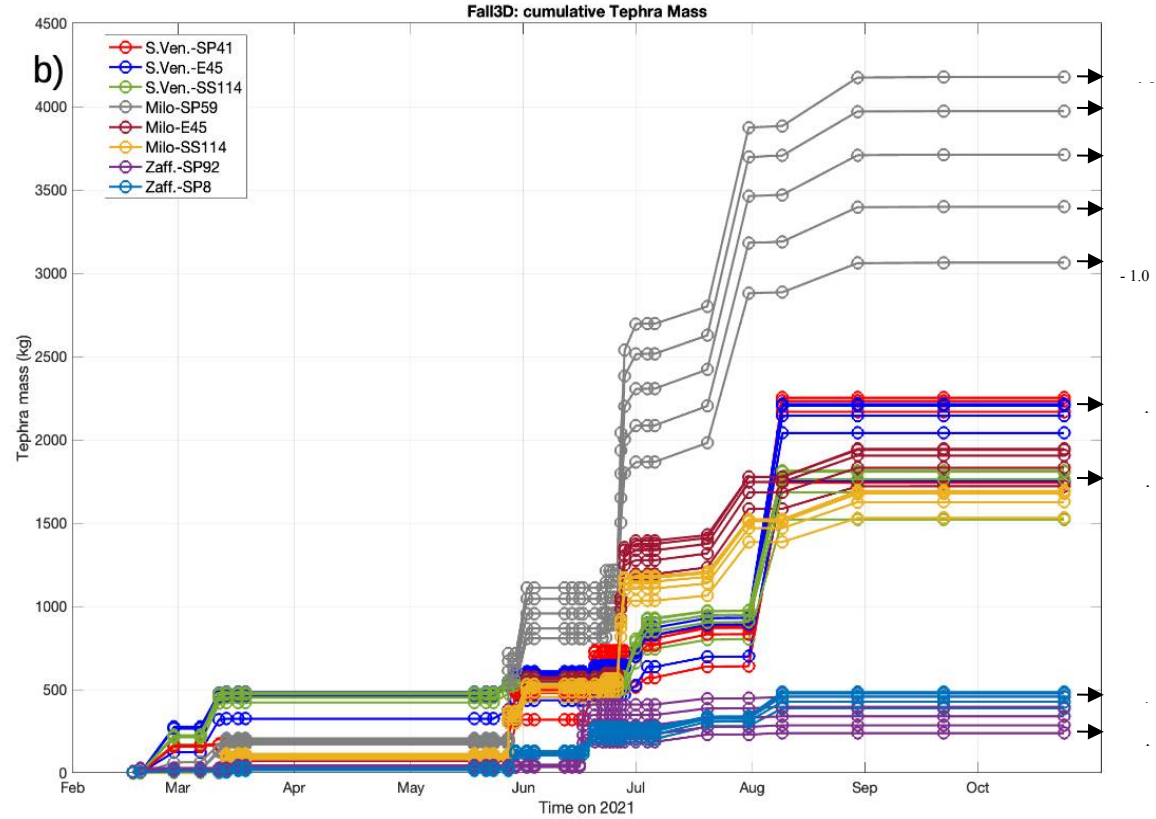
351 **4.2. Tephra mass on specific road-points**

352 We investigate how the tephra load, derived from both models, can be used to assess the accumulated tephra mass on the road
 353 network for the selected municipalities, assuming a cell size of (5×5) metres in the interpolated tephra load map. It is important
 354 to highlight that deposited tephra causes disruptions on main roads, specifically in terms of the kilometres of roadways that
 355 may face critical driving conditions. The location of the Etna volcano, along with the prevailing westerly and northwesterly
 356 winds at high altitude, favours the tephra fallout and dispersal primarily toward east (31%), southeast (35%) and north-west
 357 (29%) Etna flanks, and only (6%) directed towards south. These patterns are derived from the analysis of ERA5 reanalysis
 358 wind data during 39 eruptive events that occurred in 2021. These results are consistent with the historical statistical distribution
 359 of wind direction and relative velocity from the 1990-2007 period at altitudes between 5 and 10 km, as derived from
 360 meteorological forecast data (Barsotti et al., 2010; Scollo et al., 2013). The deposited tephra mass, derived from two models, is
 361 computed by selecting eight road-points (shown in Figure 1) across different roads in the municipalities of Milo, Santa
 362 Venerina (Sven), Zafferana Etnea (Zaff) and Giarre municipalities: provincial roads (SP41, SP92, SP8 and SP59); the highway
 363 (E45); and the state road (SS114). To increase the number of road-points on the southeast flank of Etna, we also include road-
 364 points from the E45 and SP114 in the municipality of Giarre. In Figure 5 we show the time cumulative tephra mass for different
 365 median ϕ values at specific points in the selected roads, as computed by Tephra2 (Figure 5a) and Fall3D (Figure 5b).
 366 Generally, increasing the median ϕ increases the deposited tephra mass and vice versa. Obviously, this estimate depends on the
 367 collection point, because for a given ϕ , if the mass deposited in the proximal area increases, it decreases in the distal one, since
 368 the total mass deposited is conserved. The highest simulated tephra mass values from both models are found at SP59 in Milo,
 369 with Tephra2 recording between 2750 and 3375 kg and Fall3D showing between 3000 and 4250 kg at the end of the paroxysm
 370 sequence. This location is approximately 12 km from the summit of Etna, making it the closest among the analysed points. In
 371 contrast, SP92 in Zafferana Etnea shows lower ash loads, with Tephra2 reporting about 725 to 800 kg and Fall3D indicating
 372 between 250 and 450 kg at the end of the paroxysm sequence. While Zafferana Etnea is also near Etna (12.2 km away), it is
 373 situated further south than Milo. We can evaluate these results taking into account the tolerance boundaries, usually considered
 374 as more/less five times the estimated values (Scollo et al., 2007). Indeed, the variability of tephra mass for all the road-points
 375 computed with Tephra2 ranges between limit values of 750-3375 kg, whereas the variability derived from Fall3D is between
 376 250-4250 kg. The time-cumulative function derived from Tephra2 presents larger steps in concomitance with events of 14
 377 March, 22 and 28 May, 1 July 2021 for SP59 in Milo, E45, SP49 and SS114 in Santa Venerina and SP8 in Zafferana Etnea

32

378 whereas E45 and SS114 in Milo show a larger step during the event on 24 May 2021. During the other events, the tephra mass
 379 is not large enough to generate major steps in the time-cumulative function. For most road-points, the total accumulated tephra
 380 mass stabilises at values between 500 kg and 1250 kg after the paroxysm of 20 July 2021, with the exception of SP59 in Milo.
 381 The time-cumulative function obtained with Fall3D shows larger steps during the events of 28 May, 2 and 27 June, 31 July
 382 2021 for SP59 in Milo. E45 and SS114 in Milo show a larger step on 27 June 2021, whereas SP41, E45 and SS114 in Santa
 383 Venerina exhibit a large step on 29 August 2021, and SP92 in 17 June 2021. In Zafferana Etnea, SP8 shows a time increase of
 384 tephra mass, whereas in Zafferana Etnea the tephra mass stabilises at values between 250 kg and 500 kg by the end of June. The
 385 time-cumulative tephra mass on SP41, E45 and SS114 in Santa Venerina and SS114 on Milo stabilises between 1325 kg and
 386 2075 kg starting from the beginning of August. Also in the case of Fall3D, SP59 in Milo is confirmed as the most impacted
 387 road-point due to accumulation of tephra in time where the time-cumulated tephra increases more than at the other target
 388 points, with larger steps, and then stabilises starting from August. These results suggest that, following the 2021 cluster of
 389 Etna lava fountains, the roads of Milo and Santa Venerina municipalities have been the most impacted from tephra deposition
 390 in time.



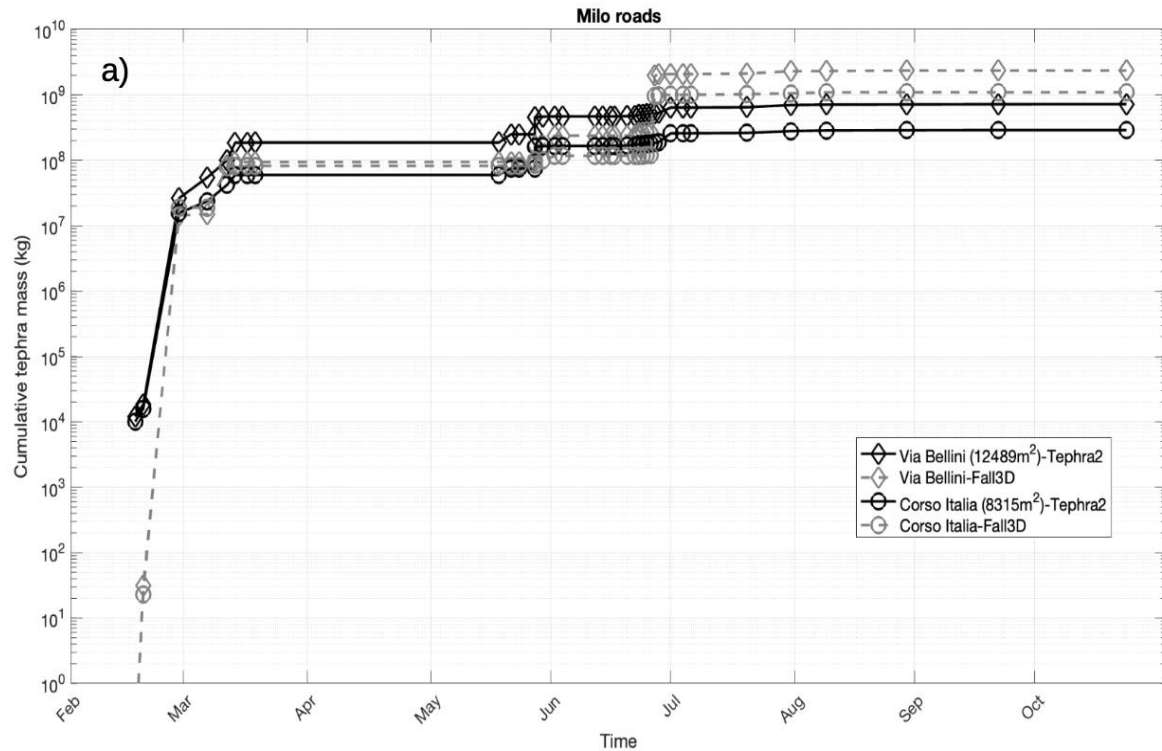


392

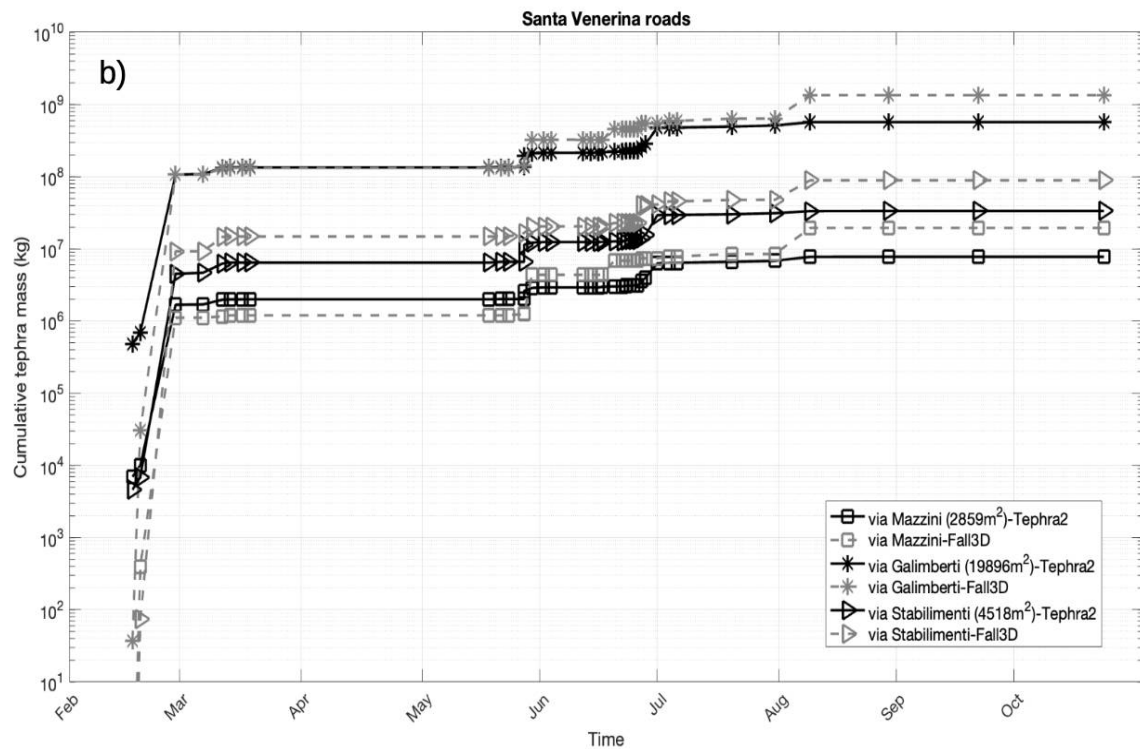
393 **Figure 5: The time series of cumulative tephra mass simulated by the Tephra2 (a) and Fall3D (b) models for all analysed explosive**
 394 **events at Etna in 2021, which shows plumes dispersing to the east and southeast. Each road-point is represented by a unique colour**
 395 **and symbol. We display the cumulative tephra mass corresponding to each road-point and varying the median value of ϕ . The larger**
 396 **the mean grain size, the higher the accumulated load for that road-point, as indicated on the right side of each figure.**

397 4.3 Total mass accumulated on selected roads

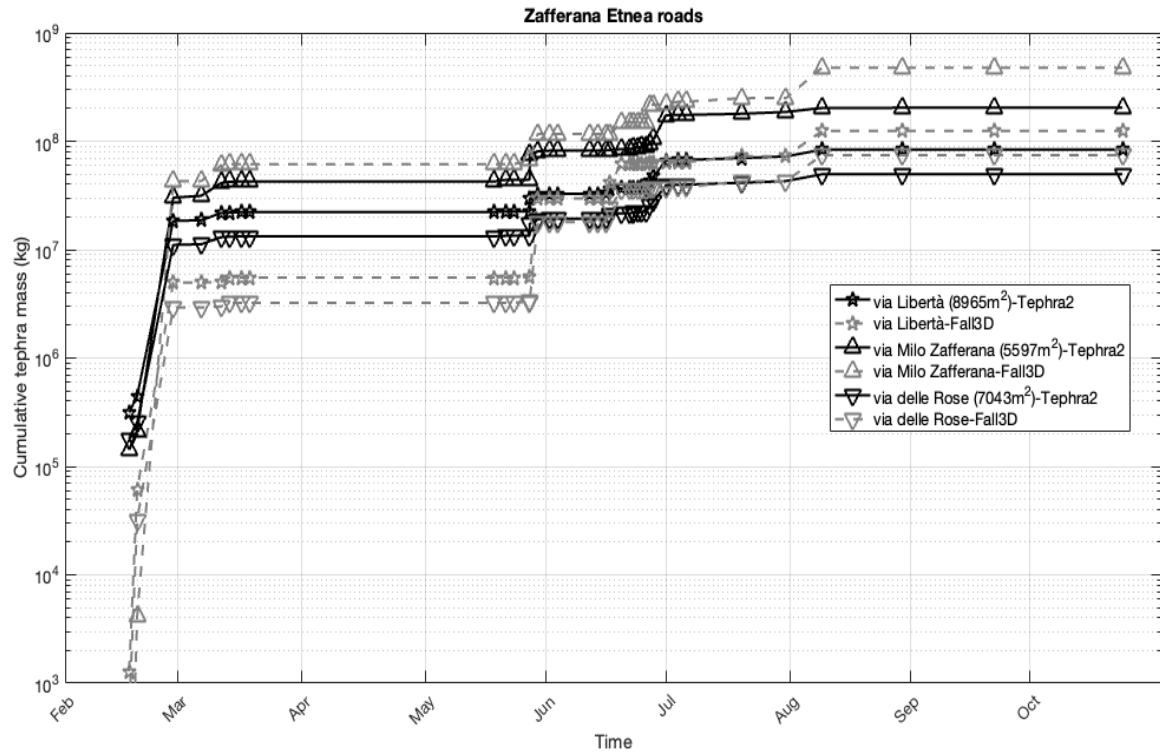
398 In this section we quantify the total tephra mass deposited on selected main roads previously listed in Table 3 for each
 399 municipality. Three panels in Figure 6a, 6b and 6c are related, respectively, to the time-cumulative mass on Milo (a), Santa
 400 Venerina (b) and Zafferana Etnea (c) computed on selected roads of known area. Analysing the panels in Figure 6 we observe
 401 some rapid increases in the cumulative trend of tephra mass mainly for the Fall3D simulations (grey dashed line) with respect
 402 to Tephra2 (dark continuous line) simulations. These rapidly increasing trends are found in Milo on 12 March, 28 May (18:10-
 403 21:10 UTC), 27 June 2021, in Santa Venerina on 30 May, 17 June 2021 and in Zafferana Etnea. Generally, all the selected
 404 roads show a large step in the estimated cumulative tephra mass on 19 February, regardless of the model used. The largest step
 405 of total mass is found around June and July, as confirmed by the plots shown in Figure 6a.



406



407

408
409

410 **Figure 6: Cumulative tephra mass on selected roads for Milo (a), Santa Venerina (b) and Zafferana Etnea (c), respectively, for all**
 411 **Etna explosive events here analysed and simulated using the Tephra2 (dark continuous line) and Fall3D (grey dashed line) models.**
 412 **Each road is plotted with different symbols and identified by the relative area (m², assuming a road width of 6 m), as listed in the**
 413 **legend.**

414 In Table 5 we summarise the total tephra mass deposited during the 39 Etna events in 2021 for the selected roads in each
 415 municipality. The last three rows show the total tephra mass computed for the complete road network of each town. The Fall3D
 416 estimates are generally larger than those from Tephra2, with the ratio ranging from 1.5 to 3.8 for the roads and from 2.0 to 5.0
 417 for the towns, though the variability can be as much as a factor of five in either direction. We observe that during about one year
 418 of Etna's paroxysms, in the nearest municipalities under examination, the estimated value of total tephra mass accumulated in
 419 the main streets ranges between 10⁶-10⁹ kg. A difference of at most one order of magnitude in the total accumulated mass
 420 according to the two models is found. It is worth noting that these values are computed under the worst condition, i.e. without
 421 considering the tephra mobilisation due to external factors, such as rain or wind, during the complete time range, as well as
 422 assuming not road cleaning after each event. Therefore, this tephra mass represents a computed estimate of the total amount of
 423 tephra mass that theoretically had to be removed to the roads and disposed of during and after the 2021 crisis.

424 **Table 5. Total mass accumulated over 39 Etna events on the selected roads for Milo, Santa Venerina and Zafferana Etnea**
 425 **municipalities, as simulated by Tephra2 and Fall3D models (fixing $\phi=0.5$ and assuming a road width of (6 ± 0.5) m). The total mass**

40

426 on the whole road network of Milo, Santa Venerina and Zafferana, for three road widths (5.5 m, 6 m, 6.5 m), is in the last three rows.

427 On the right column the mass ratio between Fall3D and Tephra2 results.

428

Location	Mass (10^7 kg)		
	Tephra2 (5.5, 6, 6.5 m-width road)	Fall3D (5.5, 6, 6.5 m-width road)	Mass Ratio
Milo-Via V. Bellini	66.2, 72.2, 78.2	216.3, 235.9, 255.6	3.3
Milo-Corso Italia	26.6, 29.0, 31.3	100.8, 109.9, 119.1	3.8
S. Venerina-Via G. Mazzini	0.09, 0.7, 0.8	0.2, 1.8, 2.1	2.6
S. Venerina-Via D. Galimberti	52.4, 57.0, 61.9	123.7, 134.6, 146.2	2.4
S. Venerina-Via Stabilimenti	0.8, 3.1, 3.6	2.0, 8.2, 9.7	2.6
Zafferana E.-Via Libertà	7.7, 8.4, 9.1	11.4, 12.4, 13.5	1.5
Zafferana E.-Via Zafferana Milo	18.7, 20.4, 22.1	43.7, 47.7, 51.7	2.4
Zafferana E.-Via delle Rose	4.6, 5.0, 5.4	6.8, 7.4, 8.1	1.5
Total mass on the whole road network of each municipality			
Milo	7310.7, 7975.3, 8639.9	14937.5, 16295.5, 17653.5	2.0
Santa Venerina	488.4, 805.5, 952.0	1510.4, 2641.9, 3122.3	3.3
Zafferana Etnea	5162.3, 5631.5, 6100.9	26632.4, 29053.5, 31474.6	5.0

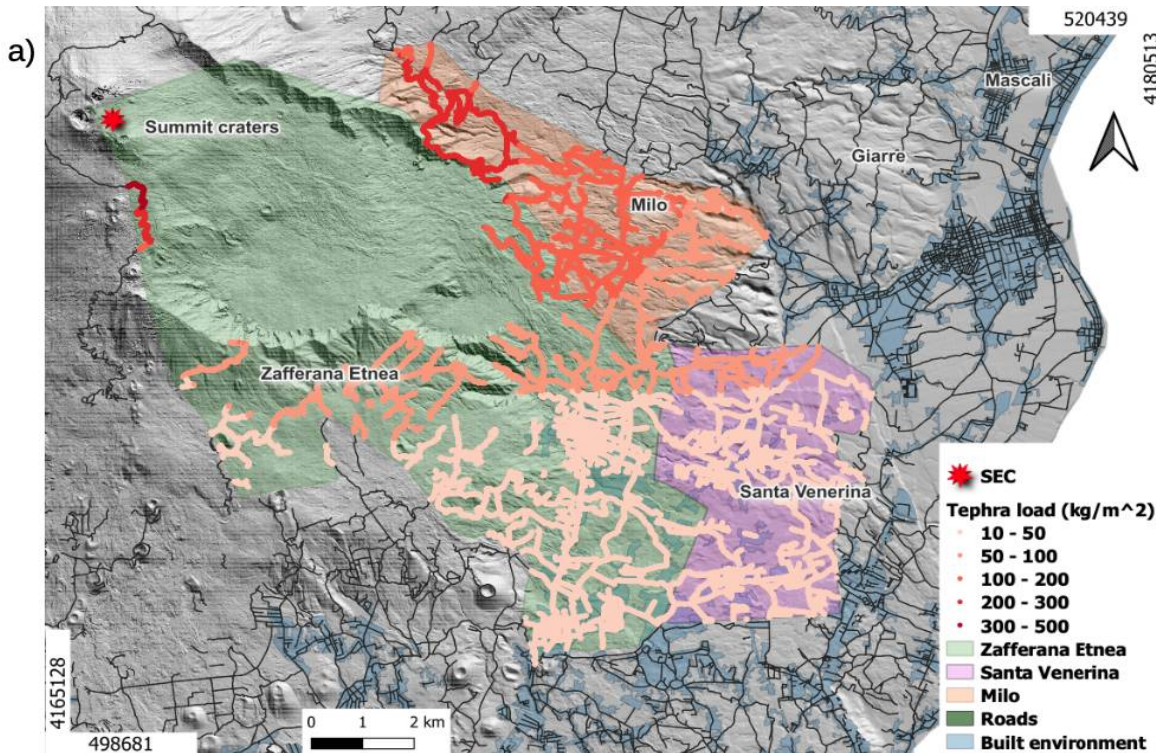
429

430 4.4 Total mass accumulated on the full road network

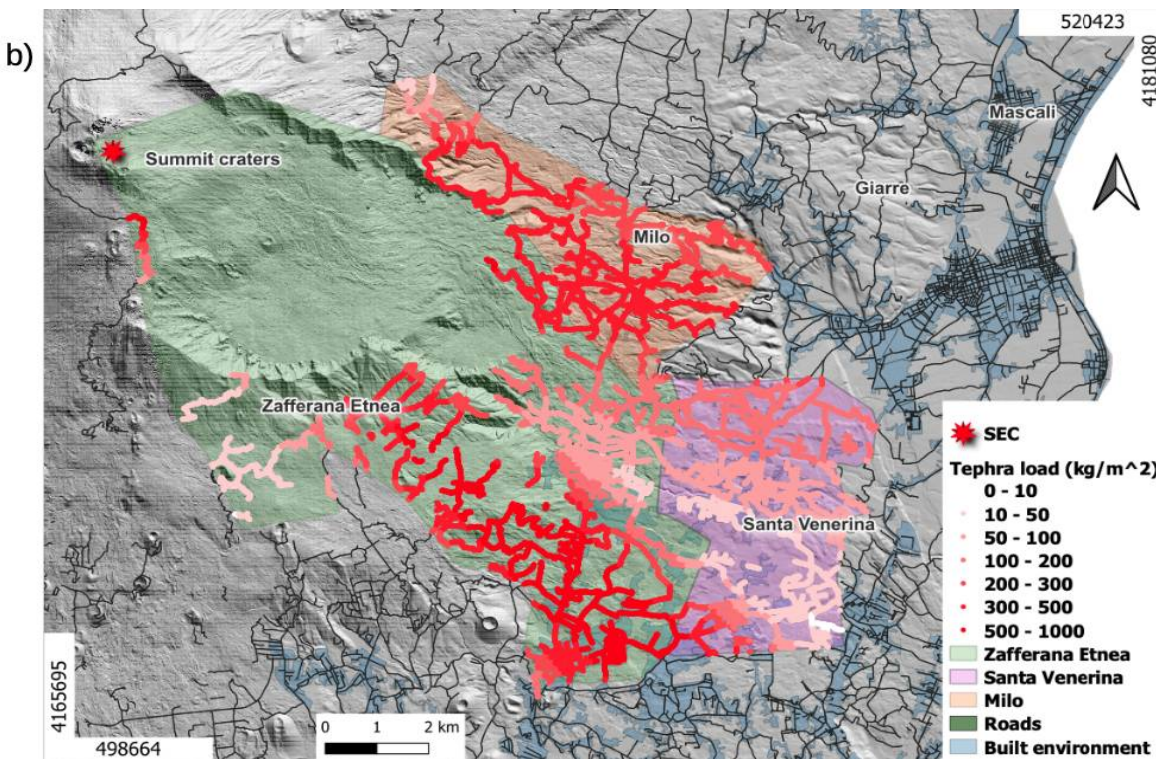
431 Similarly to Figure 3, Figure 7 shows the cumulative tephra load (kg/m^2) on the geo-referenced road map within the Milo (light
432 orange area), Santa Venerina (light pink area) and Zafferana Etnea (light green area) municipalities for all 39 Etna lava
433 fountains, computed using Tephra2 (Figure 7.a)) and Fall3D (Figure 7.b)) models.

434

435



436

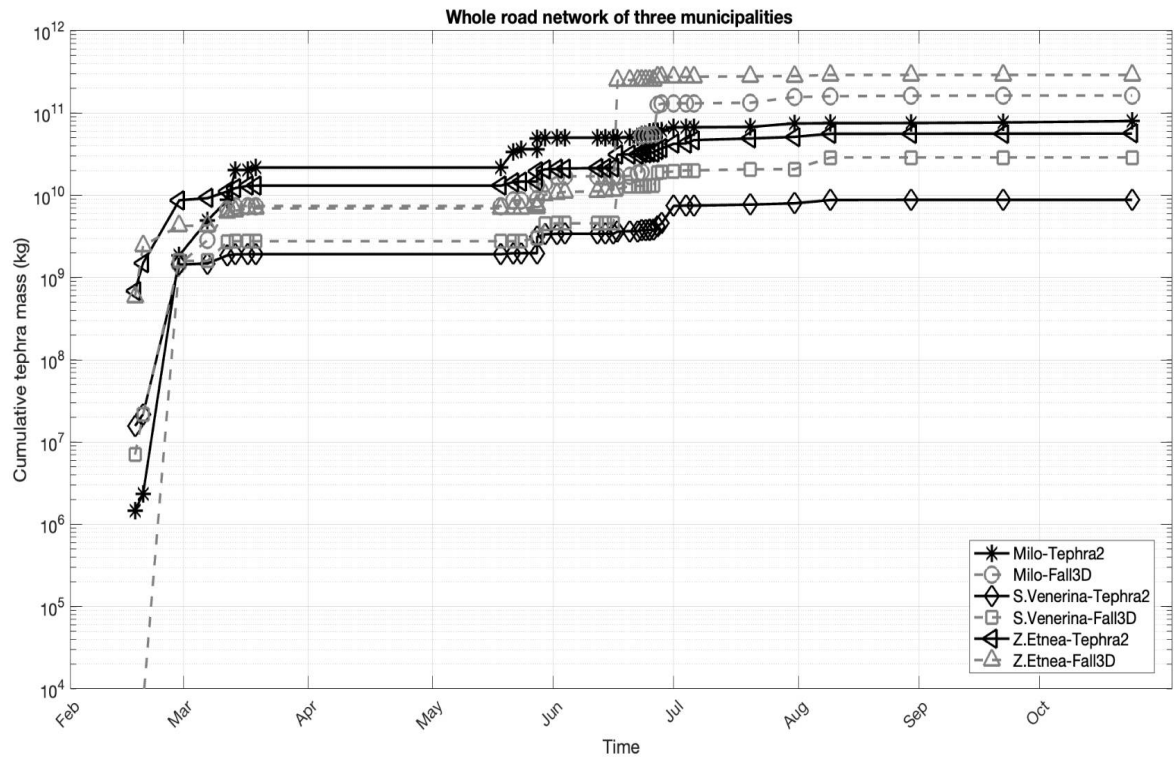


437

438 **Figure 7: Cumulative tephra load (kg/m²) for all 39 Etna lava fountains analysed in this work, computed on the whole road network**
 439 **of Milo, Santa Venerina and Zafferana Etnea using (a) Tephra2 and (b) Fall3D models, assuming $\phi=0.5$. The road graph is bold**
 440 **highlighted and in red scale coloured in function of deposited tephra values.**

441 Considering the area of each road, we compute the time-cumulative tephra mass (kg) relative to Milo, Santa Venerina and
 442 Zafferana, over the whole road network, as computed by both numerical models (Figure 8). Normally, the cumulative tephra
 443 mass derived from Tephra2 (dark continuous line) after an initial rapid growth tends to stabilise, in contrast with the trends
 444 obtained using Fall3D (grey dashed line), which present rapid increases in estimates throughout the sequence. These leaps in
 445 Milo are for the events on 28 May, 23 June (17:40-19:00 UTC) and 27 June 2021, in Santa Venerina on 28 February, 23 and 27
 446 June 2021, and in Zafferana Etnea on 28 February and 17 June 2021. The maximum value of tephra mass deposited on the
 447 whole road network in the three municipalities ranges between 10^{10} to 10^{12} kg.

448



449

450 **Figure 8: Cumulative tephra mass for all the 2021 Etna lava fountains analysed in this work, simulated using Tephra2 (dark**
 451 **continuous line) and Fall3D (grey dashed line) models, for the whole road network in Milo, Santa Venerina and Zafferana Etnea.**

452 **4.5. Analysis of variability in tephra mass results**

453 The estimates of tephra mass, as a function of uncertainty variation related to ESPs used as input to train both numerical
 454 models and the specific limitations of the two dispersal models, are already well-documented in the literature (Scollo et al.,
 455 2008b). In the present work, we evaluated the potential mass load and total mass accumulated on the road networks of several
 456 target towns. Due to the complexity of the Fall3D model, requiring significant computational resources compared to Tephra2,
 457 the number of simulations considered for each analysed eruption was limited to the GSD variability. However, the comparison
 458 between the results provided by the two models allows a first analysis of the variability in tephra mass estimates. The
 459 evaluation of the results for the case study on 28 February 2021, observed by the XWR and analysed by Pardini et al. (2021),
 460 allowed us to confirm Tephra2 as a useful numerical model for rapid assessment of tephra dispersal and deposition on road
 461 points, and for quickly evaluating the relative tephra fallout hazard. These results are consistent with the distribution of field
 462 data in relation to XWR measurements and model outcomes shown in Figure 4a, 4b, and 4c. The Kendall's tau correlation
 463 coefficient and the MAPE presented in Table 4 further support our findings. We also highlight the high performance of XWR
 464 in measuring these quantities, although these observations are not always available in real-time. By shifting focus from
 465 individual road points to selected roads for the same Etna eruption event on 28 February 2021, we observe that the Fall3D
 466 estimates are approximately comparable with those of Tephra2, as confirmed by a ratio ranging from 0.3 to 2. When
 467 considering the entire sequence of 39 Etna eruptive events, Fall3D estimates are higher than Tephra2 for the main roads in the
 468 three municipalities and for the entire road network selected in this work. Furthermore, assuming a variability of road width
 469 (± 0.5 m) in our computations, we estimate a variability in tephra mass of approximately $\pm 9\%$. All of this information allows us
 470 to outline a more comprehensive framework for estimating the mass of tephra accumulated on roads, which is essential for
 471 managing the impact of volcanic eruptions.

472 **5. Discussion and conclusions**

473 Considering the question about the quantification of the total tephra mass deposited in a given infrastructure of interest
 474 following an (or a series of) explosive volcanic eruption(s), in this work we assessed, for the first time, the cumulated tephra
 475 mass on the road networks in three selected towns on Etna's eastern flank during several paroxysms that occurred in 2021. This
 476 accumulated mass is a theoretical estimate of the amount of material that had to be removed from the roads and disposed of
 477 during the 2021 volcanic activity. We have focussed on three target municipalities located on the east flank, i.e. Milo, Santa
 478 Venerina and Zafferana Etnea. According to the law at the time of the eruption, such material had to be handled and disposed
 479 of as special waste (Art. 35 decreto legge 77/2021). At the time of writing this paper a new law allows the use of this material
 480 for other purposes (DA n.8/Gab. 22/04/2024, <https://www.regione.sicilia.it>) as, for example, building construction. Processing
 481 measurements derived from visible and thermal cameras of INGV-OE, and, when available, from SEVIRI images and the
 482 XWR data, we can retrieve the main ESPs, useful inputs to run numerical models. In this way we can simulate and evaluate the

483 cumulated tephra load on roads in time. Processing these results with the QGIS tool, we are able to identify the roads more
484 exposed to tephra deposition. We consider that the results of this analysis can be a valuable source of information to support the
485 management of volcanic crises and for planning the reinstatement of road networks after a crisis.

486 It is known that effective and realistic transport management strategies are essential into volcanic contingency planning in
487 sectors where key infrastructure are at risk, such as the road networks. Evaluating tephra mass using two (or more) different
488 models allows assessing epistemic uncertainty, to estimate the different sensitivity of each model to same input ESPs and the
489 variability of the median ϕ . It is worth highlighting that in this work, we have neglected the uncertainties in the ESP values
490 (such as Q_M , TEM and H_{TP}), but this analysis is already available in literature (see e.g., Scollo et al., 2008b). However, these
491 values are affected by various sources of uncertainty, including pre- and post-processing of data, as well as instrument
492 sensitivity and accuracy, all of which can significantly impact the model outputs (see e.g., Mereu et al., 2023). This can lead to
493 larger uncertainties in the simulated tephra load in addition to those related to the different model settings and the physical
494 assumptions implemented in each numerical model.

495 In this work we are not considering the effect of rain which can remain trapped in the tephra deposit. Furthermore, depending
496 on the rain's intensity, the road traffic safety can worsen (e.g., by making the transport network particularly slippery) or can be
497 improved (e.g., by washing the road surface from the ash deposit). Specific thresholds of tephra load that can damage the main
498 roads system, and the necessary actions to mitigate the tephra effects are defined and known in the literature (e.g. Jenkins et al.
499 2015; Bonadonna et al. 2021b; Table 8 in Bonadonna et al., 2021a).

500 As a final consideration, we point out the importance of the validation of the results of tephra load simulation obtained with
501 two different numerical models by comparing their output with ground sampling data (in our case available from Pardini et al.,
502 2023) as well as with the XWR retrievals for the Etna explosive activity on February 28, 2021. The tephra deposit estimations,
503 as listed in Tables 2 and 3, highlight the good agreement among the ground sampling, XWR retrievals and the output of
504 numerical models. This observation makes us confident to use the two different models in evaluating not only qualitatively but
505 also quantitatively the tephra deposited during recent Etna paroxysms. In this way it is possible to provide plausible values of
506 ground cumulated tephra mass on roads, and identify which routes in the road network of the target towns may be most
507 impacted in next eruptions.

508 We consider that the analyses and the results proposed in this paper provide interesting inputs for supporting decision making
509 and crisis management. Indeed, such analyses may support planning for clean-up following volcanic eruptions, which is
510 essential for effective volcanic risk management (Hayes et al., 2019). Post-eruption clean-up of tephra deposits on roads is a
511 widespread and costly activity, both in terms of time and resources, and frequently it is an unplanned activity (Hayes et al.,
512 2019). Combining different cleaning methods, such as sweeping, suction, spraying and air blasting, could help speed up tephra
513 fallout removal from high-priority roads used in the management of these events, especially before markings are fully covered
514 (with thickness ranging from 1 to 10 mm), in order to ensure safety during cleaning operations. Understanding the economic
515 impact on affected areas (Hayes et al., 2015; Magill et al., 2006) also contributes to better risk management. Geospatial

516 analysis methods are well-documented in the literature for estimating the duration of roads cleaning-up (Hayes et al., 2017),
 517 although these operations are influenced by complex interactions between physical factors (e.g. erupted volume, column
 518 height, grain-size, wind speed and direction, and rainfall) and social factors (e.g. social priorities, prior planning, previous
 519 experience, and infrastructure interdependencies) (Hayes et al., 2015). Moreover, the presented results may support decision
 520 makers in different ways e.g. for planning and consequently for better management of a future volcanic crisis due to explosive
 521 activity of Etna volcano, as well as for getting valuable information about the order of magnitude of the total mass of tephra
 522 available for preparing the subsequent disposal and/or reuse.

523

524 **Acknowledgments:** This work was performed in the framework of the INGV Project “Pianeta Dinamico”
 525 (D53J19000170001), funded by MUR (“Ministero dell’Università e della Ricerca, Fondo finalizzato al rilancio degli
 526 investimenti delle amministrazioni centrali dello Stato e allo sviluppo del Paese, legge 145/2018”). Fall3D simulations have
 527 been performed thanks to the computational resources of the ADA cluster of Istituto Nazionale di Geofisica e Vulcanologia,
 528 Sezione di Bologna. Manuel Stocchi was funded by the “PNIR - Programma Nazionale Infrastrutture di Ricerca” with the
 529 CIR01_00013 project. C. Bonadonna was funded by SNSF project #200021_188757.

530 **References**

531 Ágústsdóttir, A. M.: Ecosystem approach for natural hazard mitigation of volcanic tephra in Iceland: building resilience
 532 and sustainability. *Nat. Hazards* 78, 1669–1691. doi: 10.1007/s11069-015-1795-6, 2015.

533 Alparone, S., Andronico, D., Lodato, L., and Sgroi, T.: Relationship between tremor and volcanic activity during the
 534 Southeast Crater eruption on Mount Etna in early 2000, *J. Geophys. Res.*, 108 (B5), 2241, doi:10.1029/2002JB001866, 2003.

535 Andronico, D.; Cannata, A.; Di Grazia, G.; Ferrari, F.: The 1986–2021 paroxysmal episodes at the summit craters of Mt.
 536 Etna: Insights into volcano dynamics and hazard. *Earth-Sci. Rev.*, 220, 103686, 2021.

537 Aravena, A., Carparelli, G., Cioni, R., Prestifilippo, M., & Scollo, S.: Toward a real-time analysis of column height by
 538 visible cameras: an example from mt. Etna, in Italy. *Remote Sensing*, 15(10), 2595, 2023.

539 Barsotti, S., Andronico, D., Neri, A. Del Carlo, P., Baxter, P.J., W.P. Aspinall, W.P., Hincks, T.: Quantitative assessment
 540 of volcanic ash hazards for health and infrastructure at Mt. Etna (Italy) by numerical simulation. *Journal of Volcanology and*
 541 *Geothermal Research* 192, 85–96, 2010.

542 Barsotti, S., Di Renzo, D.I., Thordarson, T., Björnsson, B.B. and Karlsdóttir S.: Assessing Impact to Infrastructures Due to
 543 Tephra Fallout From Öræfajökull Volcano (Iceland) by Using a Scenario-Based Approach and a Numerical Model, *Front.*
 544 *Earth Sci.* 6:196, doi: 10.3389/feart.2018.00196, 2018.

545 Baxter., P.: Medical effects of volcanic eruptions. *Bull. Volcanology*, 52, 532, doi: 10.1007/BF00301534, 1990.

546 Bebbington, M., Cronin, S. J., Chapman, I., and Turnera, M. B.: Quantifying volcanic ash fall hazard to electricity
 547 infrastructure. *J. Volcanol. Geother. Res.* 177:4, doi: 10.1016/j.jvolgeores.2008.07.023, 2008.

548 Biass S., Bonadonna C., Traglia F. et al: Probabilistic evaluation of the physical impact of future tephra fallout events for
549 the Island of Vulcano, Italy. *Bull Volcanol* 78:1–22, <https://doi.org/10.1007/s00445-016-1028-1>, 2016.

550 Biass, S., Todde A., Cioni R., Pistoletti M., Geshi N., Bonadonna C.: Potential impacts of tephra fallout from a large-scale
551 explosive eruption at Sakurajima volcano, Japan, *Bull Volcanol* 79:73 DOI 10.1007/s00445-017-1153-5, 2017.

552 Blake, D.M.; Wilson, T.M.; Gomez, C.: Road marking coverage by volcanic ash. *Environ. Earth Sci.* 75, 1–12, 2016.

553 Blake, D. M., Wilson T. M., Cole J. W., Deligne N. I. and Lindsay, J. M.: Impact of Volcanic Ash on Road and Airfield
554 Surface Skid Resistance, *Sustainability* 2017, 9, 1389, doi: 10.3390/su9081389, 2017.

555 Blong, R.J. *Volcanic Hazards: A Sourcebook on the Effects of Eruptions*; Academic Press Inc.: Sydney, Australia, 1984.

556 Blong, R. J.: *Volcanic hazards risk assessment, Monitoring and Mitigation of Volcano Hazards*, eds R. Scarpa and R. I.
557 Tilling (Berlin: Springer), 1996.

558 Bonadonna, C., C. B. Connor, B. F. Houghton, L. Connor, M. Byrne, A. Laing, and T. K. Hincks: Probabilistic modeling of
559 tephra dispersal: Hazard assessment of a multiphase rhyolitic eruption at Tarawera, New Zealand, *J. Geophys. Res.*, 110,
560 B03203, doi:10.1029/2003JB002896, 2005.

561 Bonadonna, C.: Probabilistic modelling of tephra dispersal, in: *Statistics in Volcanology*, edited by: Mader, H., Cole, S.,
562 and Connor, C. B., IAVCEI Series, Volume 1, Geological Society of London, 2006.

563 Bonadonna C, Frischknecht C, Menoni S, Romerio F, Gregg CE, Rosi M, Biass S, Asgary A, Pistoletti M, Guobadia D.,
564 Gattuso A., Ricciardi A, Cristiani C.: Integrating hazard, exposure, vulnerability and resilience for risk and emergency
565 management in a volcanic context: the ADVISE model, *Journal of Applied Volcanology*, <https://doi.org/10.1186/s13617-021-00108-5>, 2021a.

566 Bonadonna C, Biass S, Menoni S, Chris EG: Assessment of risk associated with tephra-related hazards, In: Papale, P (Ed.),
567 Forecasting and Planning for Volcanic Hazards, Risks, and Disasters: Elsevier, 329–378. (Hazards and Disasters), 2021b.

568 Calvari, S.; Cannavò, F.; Bonaccorso, A.; Spampinato, L.; Pellegrino, A.G.: Paroxysmal Explosions, Lava Fountains and
569 Ash Plumes at Etna Volcano: Eruptive Processes and Hazard Implications. *Front. Earth Sci.* 6, 107,
570 <https://doi.org/10.3389/feart.2018.00107>, 2018.

571 Calvari, S., Bonaccorso, A., Ganci, G.: Anatomy of a Paroxysmal Lava Fountain at Etna Volcano: The Case of the 12
572 March 2021, Episode. *RemoteSensing*, 13, 3052. <https://doi.org/10.3390/rs13153052>, 2021.

573 Calvari, S.; Biale, E.; Bonaccorso, A.; Cannata, A.; Carleo, L.; Currenti, G.; Di Grazia, G.; Ganci, G.; Iozzia, A.; Pecora,
574 E.; et al.: Explosive Paroxysmal Events at Etna Volcano of Different Magnitude and Intensity Explored through a
575 Multidisciplinary Monitoring System. *Remote Sens.*, 14, 4006, <https://doi.org/10.3390/rs14164006>, 2022(a).

576 Calvari, S.; Nunnari, G.: Comparison between Automated and Manual Detection of Lava Fountains from Fixed Monitoring
577 Thermal Cameras at Etna Volcano, Italy. *Remote Sens.*, 14, 2392. <https://doi.org/10.3390/rs14102392>, 2022 (b).

578 Casadevall, T. J.: The 1989–1990 eruption of redoubt volcano, Alaska: impacts on aircraft operations, *J. Volcanol.*
579 *Geother. Res.* 62, 301–316. doi: 10.1016/0377-0273(94)90038-8, 1994.

581 Connor, L. G. and Connor, C. B.: Inversion is the key to dispersion: Understanding eruption dynamics by inverting tephra
 582 fallout, in: *Statistics in Volcanology*, Society for Industrial and Applied Mathematics, Special Publication of IAVCEI N. 1,
 583 Mader, H., Cole, S., and Connor, C. B., 231–242, Geological Society, London, 2006.

584 Corradini, S., Guerrieri, L., Lombardo, V., Merucci, L., Musacchio, M., Prestifilippo, M., Scollo, S., Silvestri, M., Spata,
 585 G., Stelitano, D.: Proximal monitoring of the 2011-2015 Etna lava fountains using MSG-SEVIRI data. *Geosciences* 8, 140,
 586 2018.

587 Costa A., G. Macedonio a, A. Folch: A three-dimensional Eulerian model for transport and deposition of volcanic ashes,
 588 *Earth and Planetary Science Letters* 241, 634–647, 2006.

589 Costa, A., Folch, A., Macedonio, G., Giaccio, B., Isaia, R., and Smith, V. C.: Quantifying volcanic ash dispersal and impact
 590 of the Campanian Ignimbrite super-eruption, *Geophysical Research Letters*, 39, <https://doi.org/10.1029/2012GL051605>,
 591 2012.

592 Dominguez, L., Bonadonna, C., Frischknecht, C., Menoni, S. and Garcia, A.: Integrative Post-event Impact Assessment
 593 Framework for Volcanic Eruptions: A Disaster Forensic Investigation of the 2011–2012 Eruption of the Cordón Caulle
 594 Volcano (Chile). *Front. Earth Sci.* 9:645945. doi: 10.3389/feart.2021.645945, 2021.

595 Freret-Lorgeril, V., Bonadonna, C., Corradini, S., Donnadieu, F., Guerrieri, L., Lacanna, G., Marzano, F.S., Mereu, L.,
 596 Merucci, L., Ripepe, M., et al.,: Examples of Multi-Sensor Determination of Eruptive Source Parameters of Explosive Events
 597 at Mount Etna. *RemoteSensing*, 13, 2097. <https://doi.org/10.3390/rs13112097>, 2021.

598 Folch, A., Costa A, Macedonio G.: FALL3D: A computational model for transport and deposition of volcanic ash.
 599 *Computers and Geosciences* 35, 1334–1342, 2009.

600 Folch, A., Costa, A, Basart, S.: Validation of the FALL3D ash dispersion model using observations of the 2010
 601 Eyjafjallajökull volcanic ash clouds, *Atmospheric environment* volume 48, Pages 165-183, 2012.

602 Folch, A., Costa, A., and Macedonio, G.: FPLUME-1.0: An integral volcanic plume model accounting for ash aggregation,
 603 *Geosci. Model Dev.*, 9, 431–450, <https://doi.org/10.5194/gmd-9-, 2016>.

604 Folch, A., Mingari, L., Gutierrez, N., Hanzich, M., Macedonio, G. and Costa, A.: FALL3D-8.0: a computational model for
 605 atmospheric transport and deposition of particles, aerosols and radionuclides – Part 1: Model physics and numerics,
 606 <https://doi.org/10.5194/gmd-13-1431, 2020>.

607 Gordon, K.D.; Cole, J.W.; Rosenberg, M.D.; Johnston, D.M.: Effects of volcanic ash on computers and electronic
 608 equipment. *Nat. Hazards*, 34, 231–262, 2005.

609 Guffanti, M., Mayberry, G. C., and Casadevall, T. J.: Volcanic hazards to airports. *Nat. Hazards* 51, 287–302. doi:
 610 10.1007/s11069-008-9254-2, 2009.

611 Hayes, J. L., Wilson, T. M. and Magill, C.: Tephra fall clean-up in urban environments, *Journal of Volcanology and*
 612 *Geothermal Research* 304, 359–377, 2015.

613 Hayes, J., Wilson, T.M., Deligne, N.I., Cole, J., Hughes, M.: A model to assess tephra clean-up requirements in urban
 614 environments. *J. Appl. Volcanology*, 6:1. <https://doi.org/10.1186/s13617-016-0052-3>, 2017.

615 Hayes, J. L., Wilson, T. M., Carol Stewart, C., Villarosa, G., Salgado, P., Beigt, D., Outes, V., Deligne, N. I., and Leonard,
 616 G. S.: Tephra clean-up after the 2015 eruption of Calbuco volcano, Chile: a quantitative geospatial assessment in four
 617 communities, *Journal of Applied Volcanology*, 8:7 <https://doi.org/10.1186/s13617-019-0087-3>, 2019.

618 Hayes, J.L., Biass, S., Jenkins, S.F. et al. Integrating criticality concepts into road network disruption assessments for
 619 volcanic eruptions. *J Appl. Volcanol.* 11, 8, <https://doi.org/10.1186/s13617-022-00118-x>, 2022.

620 Heiken, G.; Murphy, M.; Hackett, W.; Scott, W.: Volcanic Hazards to Energy Infrastructure-Ash Fallout Hazards and
 621 Their Mitigation; World Geothermal Congress: Florence, Italy, pp. 2795–2798, 1995.

622 Hersbach, H., Bell, B., Berrisford, B., Biavati, P., Horányi, A., Muñoz Sabater, J., Nicolas, J., Peubey, C., Radu, R.,
 623 Rozum, I., Schepers, D., Simmons, A., Soci, C., Dee, D., and Thépaut, J.: ERA5 hourly data on
 624 pressure levels from 1959 to present, 1999–2049, <https://doi.org/10.24381/cds.b>, 2018.

625 Horwell, C.J. and Baxter, P.J.: The Respiratory Health Hazards of Volcanic Ash: A Review for Volcanic Risk Mitigation.
 626 *Bulletin of Volcanology*, 69, 1-24, <http://dx.doi.org/10.1007/s00445-006-0052-y>, 2006.

627 Jenkins S.F., Spence R.J.S., Fonseca J.F.B.D., Solidum R.U., Wilson T.M.: Volcanic risk assessment: quantifying physical
 628 vulnerability in the built environment. *J Volcanol Geotherm Res* 276:105–120, 2014.

629 Jenkins, S., Barsotti, S., Hincks, T. K., Neri, A., Phillips, J. C., Sparks, R. S. J., et al.: Rapid emergency assessment of ash
 630 and gas hazard for future eruptions at Santorini Volcano, Greece. *J. Appl. Volcanol. Soc. Volcanoes* 20154:16. doi:
 631 [10.1186/s13617-015-0033-y](https://doi.org/10.1186/s13617-015-0033-y), 2015.

632 Johnston, D.M.; Daly, M.: Auckland erupts!!, *N. Z. Sci. Mon.* 1995, 8, 6–7, 1995.

633 Johnston, D.M.: Physical and Social Impacts of Past and Future Volcanic Eruptions in New Zealand. Ph.D. Thesis, Massey
 634 University, Palmerston North, New Zealand, 1997.

635 Labadie, J.R.: Volcanic Ash Effects and Mitigation. Adapted from a Report Prepared in 1983 for the Air Force Office of
 636 Scientific Research and the Defence Advanced Research Projects Agency, 1994.

637 Magill, C., Blong, R. and McAneney, J.: VolcaNZ - A volcanic loss model for Auckland, New Zealand, *Journal of
 638 Volcanology and Geothermal Research* 149 (2006) 329–345, 2006.

639 Marzano, F. S., Picciotti, E., Vulpiani, G., Montopoli, M.: Synthetic signatures of volcanic ash cloud particles from X-band
 640 dual-polarization radar. *IEEE Transactions on Geoscience and Remote Sensing*, 50(1), 193–211.
 641 <https://doi.org/10.1109/TGRS.2011.2159225>, 2012.

642 Marzano, F. S., Mereu, L., Scollo, S., Donnadieu, F., Bonadonna, C.: Tephra mass eruption rate from ground-based X-band
 643 and L-band microwave radars during the November 23, 2013 Etna Paroxysm. *IEEE Transactions on Geoscience and Remote
 644 Sensing*, 58(5), 3314–3327, <https://doi.org/10.1109/tgrs.2019.2953167>, 2020.

645 Mastin, L. G., Guffanti, M., Servranckx, R., Webley, P., Barsotti, S., Dean, K., et al.: A multidisciplinary effort to assign
 646 realistic source parameters to models of volcanic ash-cloud transport and dispersion during eruptions. *Journal of Volcanology*
 647 and *Geothermal Research*, 186(1–2), 10–21, <https://doi.org/10.1016/j.jvolgeores.2009.01.008>, 2009.

648 Mereu, L., Marzano, F. S., Montopoli, M., Bonadonna, C.: Retrieval of tephra size spectra and mass flow rate from C-band
 649 radar during the 2010 Eyjafjallajökull eruption, Iceland. *IEEE Transactions on Geoscience and Remote Sensing*, 53(10),
 650 5644–5660. <https://doi.org/10.1109/tgrs.2015.2427032>, 2015.

651 Mereu, L., Scollo, S., Bonadonna, C., Freret-Lorgeril, V., Marzano, F. S.: Multisensor characterization of the incandescent
 652 jet region of lava fountain-fed tephra plumes. *Remote Sensing*, 12(21), 3629. <https://doi.org/10.3390/rs12213629>, 2020.

653 Mereu, L., Scollo, S., Bonadonna, C., Donnadieu, F., Freret Lorgeril, V., Marzano, F. S.: Ground-based remote sensing of
 654 volcanic mass flow: Retrieval techniques and uncertainty analysis of Mt. Etna eruptions in 2015. *IEEE Journal of Selected*
 655 *Topics in Applied Earth Observations and Remote Sensing*, 15, 504–518, <https://doi.org/10.1109/jstars.2021.3133946>, 2022.

656 Mereu, L., Scollo, S., Garcia, A., Sandri, L., Bonadonna, C., Marzano, F. S.: A new radar-based statistical model to
 657 quantify mass eruption rate of volcanic plumes. *Geophysical Research Letters*, 50, e2022GL100596, <https://doi.org/10.1029/2022GL100596>, 2023.

659 Miller, T.P.; Casadevall, T.J.: Volcanic ash hazards to aviation. In *Encyclopedia of Volcanoes*, 1st ed.; Sigurdsson, H.,
 660 Houghton, B., Rymer, H., Stix, J., McNutt, S., Eds.; Academic Press: San Diego, CA, USA, pp. 915–930, 1999.

661 Montopoli, M.: Velocity profiles inside volcanic clouds from three-dimensional scanning microwave dual-polarization
 662 Doppler radars. *Journal of Geophysical Research: Atmospheres*, 121(13), 7881–7900, <https://doi.org/10.1002/2015JD023464>, 2016.

664 Pardini F., De' Michieli Vitturi M., Andronico D., Esposti Ongaro T., Cristaldi A. and Neri A.: Real-time probabilistic
 665 assessment of volcanic hazard for tephra dispersal and fallout at Mt. Etna: the 2021 lava fountain episodes, *Bulletin of*
 666 *Volcanology*, 85:6, <https://doi.org/10.1007/s00445-022-01614-z>, 2023.

667 Romeo, F.; Mereu, L.; Scollo, S.; Papa, M.; Corradini, S.; Merucci, L.; Marzano, F.S.: Volcanic Cloud Detection and
 668 Retrieval Using Satellite Multisensor Observations. *RemoteSens.*, 15, 888, <https://doi.org/10.3390/rs15040888>, 2023.

669 Sarna-Wojcicki, A.M.; Shipley, S.; Waitt, R.B.; Dzurisin, D.; Wood, S.H.: Areal distribution, thickness, mass, volume, and
 670 grain size of air-fall ash from the six major eruptions of 1980. In *The 1980 Eruptions of Mount Saint Helens; USGS Numbered*
 671 *Series 1250*; Lipman, P.W., Mullineaux, D.R., Eds.; U.S. Government Publishing Office: Washington, DC, USA, pp. 577–
 672 600, 1981.

673 Scollo, S., Del Carlo, P., Coltelli, M., Tephra fallout of 2001 Etna flank eruption: Analysis of the deposit and plume
 674 dispersion, *Journal of Volcanology and Geothermal Research* Volume 160, Issues 1–2, 1 February 2007, Pages 147–164,
 675 <https://doi.org/10.1016/j.jvolgeores.2006.09.007>, 2007.

676 Scollo, S., S. Tarantola, C. Bonadonna, M. Coltelli, and A. Saltelli: Sensitivity analysis and uncertainty estimation for
 677 tephra dispersal models, *J. Geophys. Res.*, 113, B06202, doi:10.1029/2006JB004864, 2008a.

678 Scollo, S., Folch, A., Costa, A.,: A parametric and comparative study of different tephra fallout models, *Journal of volcanology*
 679 and *geothermal research* 176,199-211, 2008b.

680 Scollo, S., Prestifilippo, M., Spata, G., D'Agostino, M., Coltelli, M.: Monitoring and forecasting Etna volcanic plumes.
 681 *Natural Hazards and Earth System Sciences*, 9(5), 1573–1585. <https://doi.org/10.5194/nhess-9-1573>, 2009.

682 Scollo, S., M. Coltelli, C. Bonadonna, and P. Del Carlo: Tephra hazard assessment at Mt. Etna (Italy), *Nat. Hazards Earth*
 683 *Syst. Sci.*, 13, 3221–3233, doi:10.5194/nhess-13-3221-2013, 2013.

684 Scollo S., Prestifilippo M., Bonadonna C., Cioni R., Corradini S., Degruyter W., Rossi E., Silvestri M., Biale E., Carparelli
 685 G., Cassisi C., Merucci L., Musacchio M. and Pecora E.: Near-Real-Time Tephra Fallout Assessment at Mt. Etna, Italy,
 686 *Remote Sens.*, 11, 2987; doi:10.3390/rs11242987, 2019.

687 Spence, R. J. S., Kelman, I., Baxter, P. J., Zuccaro, G., and Petrazzuoli, S.: Residential building and occupant vulnerability
 688 to tephra fall, *Natur. Hazards Earth Syst. Sci.* 5, 477–494. doi: 10.5194/nhess-5-477-2005.

689 Taddeucci, J., Edmonds, M., Houghton, B., James, M.R., Vergniolle, S.: Hawaiian and Strombolian Eruptions. *The*
 690 *Encyclopedia of Volcanoes*; Elsevier Inc.: Amsterdam, The Netherland; University of Rhode Island: Narragansett, RI, USA,
 691 pp. 485–503, 2015.

692 Tadini, A., Gouhier, M., Donnadieu, F., de'Michieli Vitturi, M., & Pardini, F.: Particle sedimentation in numerical
 693 modelling: a case study from the Puyehue-Cordón Caulle 2011 eruption with the PLUME-MoM/HYSPLIT models.
 694 *Atmosphere*, 13(5), 784, 2022.

695 Takishita, K., Poulidis, A. P., & Iguchi, M.: Tephra4D: a python-based model for high-resolution tephra transport and
 696 deposition simulations—applications at Sakurajima volcano, Japan. *Atmosphere*, 12(3), 331, 2021.

697 Volentik A.C.M., Connor C.B., Connor L.J., Bonadonna C.: Aspects of volcanic hazards assessment for the Bataan nuclear
 698 power plant, Luzon Peninsula, Philippines. In: Connor C., Chapman N.A., Connor L. (eds) *Volcanic and tectonic hazard*
 699 *assessment for nuclear facilities*. Cambridge University Press, Cambridge, 2009.

700 Vulpiani, G., Ripepe, M., Valade, S.: Mass discharge rate retrieval combining weather radar and thermal camera
 701 observations. *Journal of Geophysical Research: Solid Earth*, 121(8), 5679–5695, <https://doi.org/10.1002/2016jb013191>, 2016.

702 Wardman, J. B., Wilson, T., Bodger, P. S., Cole, J. W., and Johnston, D. M.: Investigating the electrical conductivity of
 703 volcanic ash and its effects on HV power systems. *Phys. Chem. Earth* 45–46, 128–145. doi: 10.1016/j.pce.2011.09.003, 2012.

704 Wilson, L., Parfitt, E.A., Head, J.W.: Explosive volcanic eruptions-VIII. The role of magma recycling in controlling the
 705 behaviour of Hawaiian-style lava fountains. *Geophys. J. Int.*, 121, 215–225, 1995.

706 Wilson, T. M, Stewart, C., Sword-Daniels, V., Leonard, G. S., Johnston, D. M, Cole, J. W., Wardman, J., et al.: Volcanic
 707 ash impacts on critical infrastructure. *Phys. Chem. Earth* 45–46, 5–23. doi: 10.1016/j.pce.2011.06.006, 2012.

708 Wilson, G.; Wilson, T.M.; Deligne, N.I.; Cole, J.W.: Volcanic hazard impacts to critical infrastructure: A review. *J.*
 709 *Volcanol. Geotherm. Res.*, 286, 148–182, 2014.

711

712

713